JGR Planets

RESEARCH ARTICLE
10.1029/2021JE006908

Numerical Investigation of Lunar Basin Formation Constrained by Gravity Signature

T. Lompa[1,2], K. Wünnemann[1,2], D. Wahl[3], S. Padovan[4,5], and K. Miljković[6]

[1]Department of Impact and Meteorite Research, Leibniz Institute for Evolution and Biodiversity Science, Museum für Naturkunde, Berlin, Germany, [2]Institute of Geological Sciences, Freie Universität Berlin, Berlin, Germany, [3]Department of Planetary Geodesy, Institute of Geodesy and Geoinformation Science, Technische Universität Berlin, Berlin, Germany, [4]Deutsches Zentrum für Luft- und Raumfahrt - German Aerospace Center, Institute of Planetary Research, Berlin, Germany, [5]WGS at Flight Dynamics, EUMETSAT, Darmstadt, Germany, [6]Space and Science Technology Centre, School of Earth and Planetary Science, Curtin University, Perth, WA, Australia

Abstract Impact basins on the Moon can serve as a benchmark for timing and intensity of the impact flux in the inner solar system. The basin morphology and morphometry depend on impactor size, mass, and velocity as well as the thermal state of the lunar lithosphere which is a function of the cooling history. Erosion by superimposed impact bombardment has altered the surface expression of basin structures over time, making it difficult to determine the size unequivocally solely based on topographic expression. The gravity signature of basins is thought to be a less altered measure of the size of impact structures. By a systematic study of basin formation using the iSALE-2D shock-physics code, we investigate the influence of the lunar thermal state and different impactor properties on the transient crater and final basin size and on the resulting gravity anomaly. As constraints we use gravity data of 16 farside basins and their assumed formation ages to estimate the subsurface temperature related to the cooling history of the Moon. Our modeling results confirm that the thermal state affects the basin formation process and the basin sizes significantly. We provide quantitative relationships between the observed gravity signal, the different basin sizes, and the impactor diameter considering the thermal state of the Moon upon impact, which correlates with the formation ages or periods in the literature. Our study allows for estimating the impactor size from the observed gravity field if the formation age and, thus, the thermal state of the lithosphere is approximately known.

Plain Language Summary Large basin structures testify to the lunar bombardment history by bodies several tens to hundreds of kilometers in diameter. To reconstruct how often the Moon, and thus also Earth, was hit by large cosmic bodies of a given size, it is essential to relate the size of basin structures with impactor size. However, since the surface expression of most known basins on the Moon is not pristine, the definition of the actual basin size is often ambiguous. As an alternative, we use the observed pronounced positive gravity excursion across lunar basins as a measure of basin size. In addition, we consider the thermal evolution of the Moon which is thought to affect the characteristics of the gravity signature of basins. Therefore, the timing when a given basin was formed in the cooling history of the Moon plays an important role. We use the gravity signature and the lunar thermal state as constraints for modeling the formation of the lunar basins as a function of impactor size. Our results allow for estimating the impactor size and thermal state of the Moon for 16 lunar farside basins. The predicted thermal states are in line with proposed absolute ages of the basins.

Key Points:

- We provide relationships between impactor size, gravity signal, and farside basin size as a function of cooling history and formation time
- Gravity anomalies serve as a measure of basin size as impacts altered morphology and crustal thickness models simplify subsurface structure
- Our basin formation models agree with the assumed formation time based on crater chronology and the estimated cooling history of the Moon

Supporting Information:

Supporting Information may be found in the online version of this article.

Correspondence to:

T. Lompa,
tomke.lompa@mfn.berlin

Citation:

Lompa, T., Wünnemann, K., Wahl, D., Padovan, S., & Miljković, K. (2021). Numerical investigation of lunar basin formation constrained by gravity signature. *Journal of Geophysical Research: Planets*, *126*, e2021JE006908. https://doi.org/10.1029/2021JE006908

Received 26 MAR 2021
Accepted 8 OCT 2021

1. Introduction

Impact craters are the most prominent landform on the Moon. The largest impact craters on the Moon formed during the first 700 Ma since its formation (e.g., Morbidelli et al., 2012, 2018; Wilhelms et al., 1987) and, thus, serve as an important benchmark regarding the timing and intensity of the impactor flux during this time period, often referred to as late accretion period. Topographic data from the Lunar Orbiter Laser Altimeter (Smith et al., 2010) provide insight into the morphology and morphometry of large basin structures; however, in particular, older basins have undergone substantial degradation processes by subsequent impacts. In some cases, the typical surface expression has been majorly removed, making it difficult to estimate the original size of a given structure if the crater rim or other topographic features cannot

be identified unequivocally. Younger, well-preserved basins, such as Orientale, may serve as reference in terms of basin morphology and morphometry showing an inner depression and multiple rings (e.g., Smith et al., 2017; Zuber et al., 2016). In principle, it can be assumed that basin's parameters such as, for example, the basin inner depression, spacing of the rings, and extent of the mantle uplift are related to each other (e.g., Baldwin, 1963; Head, 1974, 1977; Johnson et al., 2016; Miljković et al., 2015; Potter et al., 2015). However, strong deviations of observed parameters from the proposed systematic relationships, so-called impact scaling laws, suggest that either different degrees of erosion have distorted the morphometry–size relationships or changes in the properties of the crust related to the cooling history of the Moon affected the formation mechanism and, thus, also the basin morphometry and morphology. In particular, the latter has been shown by Miljković et al. (2016).

Due to the lack of unequivocal morphometric features as a consequence of impact-induced erosion and impact gardening, gravity data from the Gravity Recovery and Interior Laboratory (GRAIL) mission (Zuber et al., 2013) have been used as an additional parameter to estimate the size of a given basin. The majority of basin structures exhibit huge mass concentrations, recognizable by a strong positive Bouguer gravity anomaly in the center, surrounded by a negative Bouguer anomaly. Neumann et al. (2015) correlated the diameter of the central gravity anomaly with the diameter of observed ring structures of well-preserved basins, which may serve as a measure of the size of a given structure. Previously hidden basin structures that do not show any surface expression but are evident through their gravity field suggest an impact origin and have been added to the basin inventory of the Moon (Neumann et al., 2015).

Numerical modeling studies of basin formation (e.g., Ivanov et al., 2010; Johnson et al., 2018; Melosh et al., 2013; Miljković et al., 2015, 2016; Potter et al., 2015; Zuber et al., 2016) and modeling of crustal thickness (Wieczorek et al., 2013) have shown that the observed gravity signature primarily results from uplifted mantle material and associated crustal thinning in the central part of the basin and a concentric region surrounding the inner part where the crust is thicker (annular bulge) compared to the ambient crustal thickness. Detailed studies of the young and relatively pristine basin Orientale revealed that mass variations below the surface as well as the topography of the crust–mantle boundary may be more complex (Andrews-Hanna et al., 2018; Johnson et al., 2016; Potter et al., 2013; Zhu et al., 2015) and long-term processes such as cooling and isostatic adjustment associated with changes in the mass distribution may not be negligible in the interpretation of the present-day gravity signatures of impact basins (Freed et al., 2014; Melosh et al., 2013).

Temperature affects the rheological behavior of rocks, most notably by modifying their resistance to plastic deformation. Thus, the cooling history of a body influences the basin morphology through the time-dependent nature of the temperature of the crust and mantle. In the case of the Moon, where the cooling history shows a marked nearside–farside asymmetry (e.g., Laneuville et al., 2013; Spohn et al., 2001), both time location and of formation influence a basin morphology (e.g., Johnson et al., 2016; Miljković et al., 2015, 2016; Potter et al., 2015). As a consequence, the relationship between the size of a given basin and its gravity signature may also depend on when the basin was formed and where it is located.

The chronology of basin formation, based on the crater size–frequency distribution and radiogenic dating of Apollo sample material, has been proposed by, for example, Wilhelms et al. (1987) and Fassett et al. (2012) and most recently revised by Orgel et al. (2018). Coupling the formation time with thermal evolution models (e.g., Laneuville et al., 2013, 2018) may allow for a better understanding of the characteristic basin morphometry and gravity signature as a function of basin size and formation time. Previous systematic modeling studies of basin formation (Johnson et al., 2018; Miljković et al., 2015, 2016; Potter et al., 2012, 2013) consider different thermal profiles representing different times in the cooling history of the Moon and propose scaling laws relating structural data such as crustal annular bulge with basin and impactor size.

In the study, we use the observed Bouguer gravity signal of 16 basins on the lunar far side to test our models. We aim to constrain a set of model parameters that best reproduce the observed gravity signature of each of the basins we selected for this study. The free parameters in our models are the impactor diameter, the preimpact crustal thickness, and the thermal profile representing different formation times. First, we analyze the transient crater to evaluate changes in the basin-forming process during the excavation stage. Then, we relate the transient crater diameter to the Bouguer anomaly diameter to estimate the changes in

basin formation as a function of target temperature, crustal thickness, and impactor size. In a next step, we compare the Bouguer gravity anomalies from both the GRAIL mission and the numerical models of final basin formation. The best fit model for each basin is then found by employing a specific correlation method comparing the observed gravity data with the gravity signature we obtain from our formation models. The usage of the correlation method is not limited to a basin size. This approach allows for estimating the impactor size for a given basin or, in turn, constraining the formation time if a certain impactor size is assumed.

2. Methods

To investigate basin formation processes, we conducted a systematic numerical modeling study. We use the well-established iSALE-2D shock-physics code (Wünnemann et al., 2006) based on the SALE hydrocode (Amsden et al., 1980) that was successfully employed in many modeling studies of crater formation (Collins et al., 2002; Freed et al., 2014; Johnson et al., 2016; Melosh et al., 2013; Miljković et al., 2013; Potter et al., 2013; Zhu et al., 2015), benchmarked against other shock-physics codes (Pierazzo et al., 2008), and validated against experiments (Wünnemann et al., 2006). For the present study, the implemented strength, damage (Collins et al., 2004), and acoustic fluidization (AcFl; Melosh & Ivanov, 1999; Wünnemann & Ivanov, 2003) models are of particular importance.

2.1. Setup of Basin Formation Models

In our models of basin formation, we assume a half-space composed of two layers, representing the lunar crust and mantle. We account for different crustal thicknesses of 40 and 60 km which are thought to be typical for the lunar farside hemisphere (Wieczorek et al., 2013). All model parameters used in iSALE to describe the material behavior during crater formation and the initial thermodynamic state of the target for both layers are listed in Table 1 and essentially correspond to parameters used in previous studies (Collins et al., 2004; Ivanov et al., 2010; Potter et al., 2013). In our models, the impactor hits the planar target vertically with a speed of 13 km/s. The impact speed of 13 km/s corresponds to the vertical component of the mean impact velocity of 18 km/s at an angle of 45° (Le Feuvre & Wieczorek, 2011; Marchi et al., 2009); this assumption is commonly used to approximate an oblique impact, which would require a 3D simulation, by a 2D cylindrical symmetric model (Chapman & McKinnon, 1986; Elbeshausen et al., 2009) with the typical impact velocity on the Moon. We vary the impactor diameter (L_{imp}) between 20 and 100 km in steps of 10 km.

We use the Analytic Equation Of State (ANEOS; Thompson & Lauson, 1974) for dunite (Benz et al., 1989) for both the lunar mantle and the impactor and the ANEOS for basalt (Pierazzo et al., 2005) for the lunar crust to describe the thermodynamic behavior of the relevant materials. Miljković et al. (2013) and Melosh et al. (2013) point out that the choice of granitic or basaltic EOS does not make a fundamental difference in the outcome of a basin-forming process. For consistency, the chosen EOS in our study is based on previous work (Miljković et al., 2013, 2016). We employ material strength and failure models according to the implementation in iSALE by Collins et al. (2004), based on Ivanov et al. (2010), to simulate the mechanical response of crust and mantle against deformation. We also consider AcFl (Melosh, 1979; Melosh & Ivanov, 1999), which is implemented in iSALE as the so-called Block Model (Melosh & Ivanov, 1999; Wünnemann & Ivanov, 2003) to facilitate crater collapse as a consequence of temporary material weakening especially for craters in cold targets where the effect of thermal softening is less pronounced. The AcFl concept has been used in numerous previous studies of basin formation (e.g., Miljković et al., 2013; Potter et al., 2012, 2013; Zhu et al., 2015) and is not only essential to model the formation of peaks and rings in complex craters (Collins et al., 2002; Potter, 2012) but also necessary to reproduce the morphology of basins. Although it may be questionable whether AcFl is effective in the lower crust and upper mantle (e.g., Potter et al., 2013), we use this model here as well to make our simulation results comparable to previous studies. The choice of AcFl parameters follows previous models (Table 1; Potter et al., 2013; Wünnemann & Ivanov, 2003).

Additionally, we set an effective viscosity of 10^{10} Pa s for the supersolidus impact melt that is generated upon impact (Johnson et al., 2016; Potter, 2012; Potter et al., 2012, 2015; Zhu et al., 2015). We note that the total amount of melt may not be very accurate as we use the vertical component of the mean impact velocity

Table 1
Parameterization of Crust and Mantle Layers for iSALE-2D Simulations

Parameter	Crust	Mantle
Equation of state[a]	ANEOS basalt	ANEOS dunite
Thermal parameters		
Melt temperature (K)	1,360[b]	1,359[c]
Constant a in Simon approximation (GPa)	4.5[b]	3.01[c]
Exponent c in Simon approximation	3.0[b]	2.98[c]
Thermal softening model[b]		
Thermal softening	0.7	2.0
Shear strength of intact material[d]		
Poisson ratio	0.25	0.25
Coefficient of internal friction	1.1	1.58
Cohesion (MPa)	31.9	5.07
Limiting strength at high pressure (GPa)	2.47	3.26
Shear strength of damaged material[d]		
Coefficient of internal friction	0.63	0.63
Cohesion (MPa)	0.1	0.1
Limiting strength at high pressure (GPa)	2.47	3.26
Damage model[e]		
Minimum failure strain for low pressure states	1×10^{-4}	1×10^{-4}
Increase in failure strain with pressure	1×10^{-11}	1×10^{-11}
Pressure above which failure is always compressional (MPa)	300	300
Acoustic fluidization model[f]		
γ_η	0.001	0.001
γ_β	200	200
Peak vibrational velocity as a fraction of the peak particle velocity	0.1	0.1

[a]EOS based on Benz et al. (1989) and Pierazzo et al. (2005). [b]Thermal parameters based on Ivanov et al. (2010). [c]Adapted solidus for the mantle layer from Katz et al. (2003) ($T_m = 1{,}085.7°C + 132.9$ (°C/GPa) $P - 5.1$ (°C/GPa^2) P^2) using the Simon approximation from Poirier (2000) in the form of $T_m = T_0(\frac{P}{a} + 1)^{1/c}$ with melting temperature (T_m), solidus at normal pressure (T_0), constant a, and exponent c. [d]Shear strength parameters based on Potter et al. (2013). [e]Damage model parameters based on Ivanov et al. (2010). [f]AcFl model parameters based on Potter et al. (2013) and Wünnemann and Ivanov (2003).

to approximate the typical impact conditions, but we consider melt production to have little effect on the overall structural modifications by impacts.

Although the analysis of GRAIL data revealed that the porosity varies between 3% and 24% in the lunar highland crust (Wahl et al., 2020), we did not include the porosity compaction model (Wünnemann et al., 2006) in our simulations. Milbury et al. (2015) showed that the contribution of porosity in the crust to the density contrast, and, therefore, the gravity signature is dominant for impact structures smaller than 140 km in diameter. Bouguer anomalies of impact structures larger than 215 km in diameter are dominated by the mantle uplift and porosity becomes less important (Milbury et al., 2015). In our study, all investigated basins have mantle uplifts and are larger than 215 km with respect to their main ring diameter (Neumann et al., 2015). The formation process is driven by the uplift of mantle material, and, therefore, we do not expect that porosity compaction plays an important role. Additionally to the preexisting porosity in the target, the creation of new pore space during crater formation as a consequence of bulking due to shear or tensile failure is thought to have a strong effect on the gravity anomaly of impact craters. Collins (2014) shows that dilatancy (shear bulking) is important for relatively small complex craters typically showing negative Bouguer anomaly in the center. In our study, we investigate basin structures with strong positive anomalies due to mantle uplift. Obviously, both effects, the creation of porosity and, thus, reduction of density in the upper

crust and uplift of higher density mantle material, are superimposed on each other in the gravity field. Nevertheless, we think that mantle uplift clearly dominates the gravity signature due to the given size of basins in comparison to central peak craters. In addition, neglecting dilatancy allows for a better comparison of our results with previous studies (e.g., Miljković et al., 2013, 2016; Zhu et al., 2015).

We use iSALE in a grid-based Euler mode. Following previous studies, the resolution in our models is defined by the number of cells per projectile radius (CPPR). We used a resolution of 25 CPPR in all simulations. Therefore, the total number of cells of the entire computational domain varies (L_{imp} = 20 km: 700 cells · 1,104 cells [1 cell ≥ 400 m]; L_{imp} = 100 km: 615 cells · 497 cells [1 cell ≥ 2 km]) and depends on cratering efficiency which is a function of the size of the impactor and was chosen such that any effects resulting from shock wave reflections from the boundaries of the grid are negligible. In Supporting Information S1, we provide a resolution study (e.g., Wünnemann et al., 2008) to find the best compromise between accuracy and affordable computation costs for an individual model.

2.2. Preimpact Thermal Target Conditions

Previous studies (e.g., Miljković et al., 2016; Potter et al., 2013) have shown that preimpact thermal conditions in the target affect the strength of material due to thermal softening. The Moon's thermal state is related to the cooling history of the Moon; thus, it is a function of the age of the Moon. Recent studies (e.g., Orgel et al., 2018) confirm that the ages of farside basins larger than 300 km in diameter range between 3.81 Ga (the Orientale basin) and 4.31 Ga (the South Pole-Aitken basin). The studies show that most of the basins are formed between 4.07 and 4.26 Ga (e.g., Hertzsprung: ca. 4.09 Ga; Mendeleev: 4.13 Ga; Dirichlet-Jackson: 4.23 Ga; Orgel et al., 2018). To cover the time range when basins have probably formed, we split the main basin-forming period into three intervals and assign a characteristic thermal profile to each interval. Temperature profiles (Figure 1a) were obtained from thermal evolution models (e.g., Hüttig et al., 2013; Padovan et al., 2017; Figure 1) and are referred here as "warm," "intermediate," and "cold," respectively. In our study, we perform numerical modeling that is appropriate for the lunar farside hemisphere, which is considered cooler than the Procellarum KREEP Terrane (PKT) region on the nearside hemisphere or the earliest epoch of the lunar formation. For comparison, Figure 1a also includes temperature profiles used by Miljković et al. (2016).

It is also conceivable that basins have formed in an even hotter crust and partially molten upper mantle during the earliest evolution of the Moon. Miljković et al. (2021) showed that impact basins formed during the solidification of the magma ocean have different basin morphologies compared to basins formed later in time. Melt layers of different thickness placed between crust and mantle affect the interior crustal signature. Compared to models without a melt layer, the crustal thickening region gets removed and the thickness of the crustal cap in the basin center gets more prominent. By including melt layers, the central basin depression is hardly resolvable at the end of the basin formation process. But basin formation considering a lunar magma ocean and the resulting effects on gravity signature are beyond the scope of this study.

The temperature profiles (Figure 1a) are based on thermal evolution models, in which the bulk heat producing elements are divided in three reservoirs from the beginning, which in this case means after magma ocean solidification: the primary crust, an enriched KREEP layer, and the mantle. While few constraints exist at present on the thermal structure of the Moon across time, the availability, and, thus, distribution, of heat producing elements is the key driver of thermal evolution in rocky bodies. The approach taken here in modeling the thermal evolution captures a number of broad scale lunar features, namely the localized and time-limited nature of secondary crust production (i.e., volcanic activity) and the generally low magnetic field intensities associated with the KREEP terrane. As a reference, we use the model of Laneuville et al. (2013) (model 0LB in their Table 2). The resulting profiles are slightly colder than those of Laneuville et al. (2013), since we explicitly include the effect of melting on the reduction of heat sources in the mantle, following the model of Padovan et al. (2017). In these models, we adopted the anhydrous solidus parameterization of Katz et al. (2003).

The solidus after Katz et al. (2003) is included in iSALE-2D by the Simon approximation after Poirier (1991) in the form of

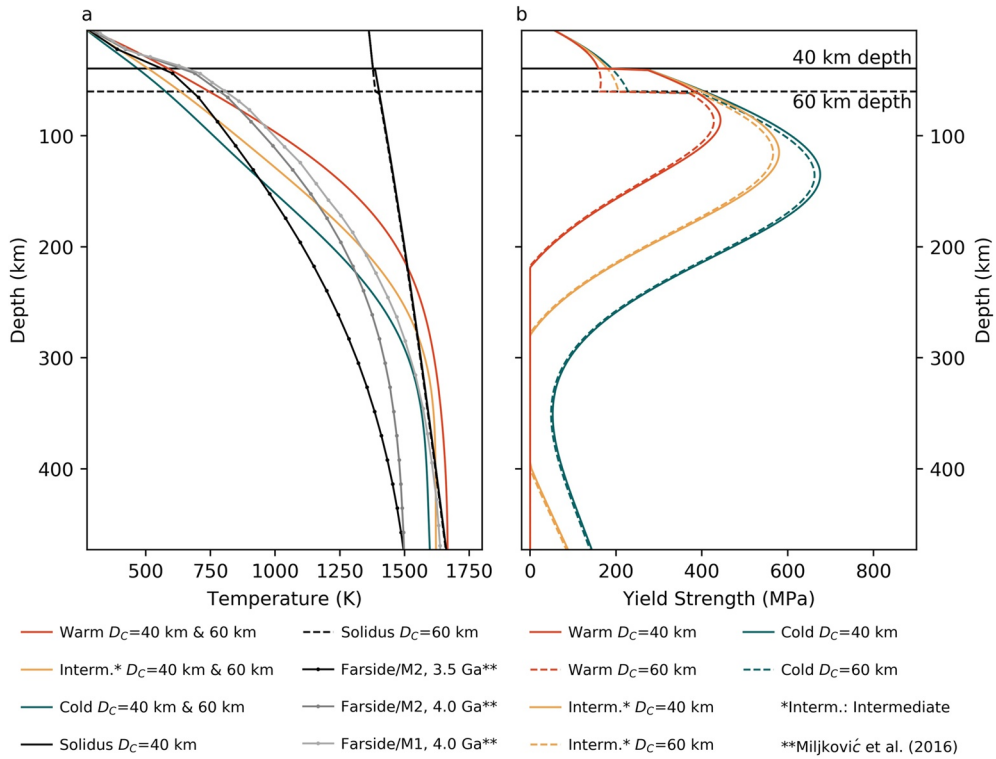

Figure 1. Temperature (a) and strength profiles (b) as a function of depth for three different thermal states of the Moon. The horizontal solid and dashed lines mark a 40 and 60 km thick crust (D_C), respectively. (a) The black curves (solid and dashed) indicate the solidus for a 40 and 60 km thick crust. Temperature profiles are based on thermal evolution models (blue, cold; yellow, intermediate; orange, warm). Solid-dotted lines (far side/M2 for 3.5 and 4.0 Ga, far side/M1 for 4.0 Ga) show the temperature profiles used in similar work by Miljković et al. (2016). (b) Solid and dashed strength profiles for the three selected temperature profiles refer to a 40 km (colored solid lines) and 60 km thick crust (colored dashed lines), respectively.

$$T_m = T_{m0}\left(\frac{P}{a}+1\right)^{1/c}, \tag{1}$$

where T_m is the melting temperature, T_{m0} melting temperature at zero pressure, P the ambient pressure, and a and c are material constants (Table 1).

As stated above, the initial thermal profile in the target influences the shear strength of the target rock and, thus, has a significant effect on lunar basin formation. Thermal softening is implemented in iSALE-2D using the strength model after Collins et al. (2004) considering a simple relationship between strength and temperature after Ohnaka (1995):

$$Y = Y_c \tanh\left(\xi\left(\frac{T_m}{T}-1\right)\right), \tag{2}$$

where Y is the thermally softened strength, Y_c is yield strength at low temperatures, T is temperature, T_m is melt temperature (solidus), and ξ is a material constant.

Figure 1b illustrates the reduction of yield strength with increasing temperature and pressure for the three thermal profiles that have been used. At depths of 40 or 60 km, the increase of yield strength indicates the transition from crust to mantle, followed by a decrease of strength at larger depths, which may be considered as the depth of the lithosphere. In parallel, ambient temperatures (T) come close to the solidus (T_m), thus lowering the strength (Y) of the material to a minimum. When ambient temperatures cross the solidus, material loses its strength and resistance against deformation completely (Potter et al., 2015).

Partially molten material is treated as strengthless but behaves as a viscous fluid. The effect of different effective viscosity on the basin formation process has been investigated by Potter (2012). Here, we follow recent studies on the formation of the Orientale basin suggesting a value of 10^{10} Pa s for the effective viscosity (Johnson et al., 2016; Zhu et al., 2015).

2.3. Lunar Basin Sizes

To reconstruct the impactor size for a given basin size, we ran 54 models of basin formation with variations of the impactor size and target temperature profiles with depth. The analysis of our models and comparison with observations is carried out in three steps: (a) we determine the size of the transient crater in our models. The results are expressed using the π-scaling laws (e.g., Holsapple, 1993); (b) we relate the transient crater size with structural features of the final crater such as the diameter of crustal thickening. In both steps, the effect of target temperature, crustal thickness, and impact energy is considered. (c) We determine the diameter of the gravity anomaly and compare it with the observed gravity anomaly of the 16 known basins.

To determine the diameter of transient craters in numerical simulations is not straightforward. This is because the gradual transition from shock wave-induced crater excavation into the gravity driven modification phase happens at different points in time along the evolving cavity. Unlike most previous studies, where the transient crater was estimated by the crater at the point in time when the crater volume reaches its maximum (e.g., Elbeshausen et al., 2009), we use an advanced method to estimate the transient crater diameter more accurately (see Supporting Information S1 and Manske et al. [2021]).

In the second step, we relate the diameter of the transient crater to the size of the final basin in our models. As stated above, it is not straightforward to determine the size of the final basin neither in our models nor at observed basin structures. The former occurs because the crater rim and major concentric faults are not well resolved in numerical models. Rather, there is a very gentle slope of the preimpact target surfaces into the basin, which makes it very difficult to determine the crater rim precisely. The latter occurs because many basin structures have been superimposed by later impact events or, in the case of multiring structures, it is not clear which morphological feature represents the actual rim diameter. Therefore, it has been suggested in previous studies (e.g., Johnson et al., 2016; Zhu et al., 2015) to use crustal thickness models—derived from satellite gravity and topography data—and the gravity signal shape itself as a measure of the size of a structure (e.g., Neumann et al., 2015). Both data sets reveal that the basin center contains an uplift of mantle material, covered by a partially thinned crust, and enclosed by a region of relatively thick crust (Neumann et al., 2015). Following previous approaches (e.g., Miljković et al., 2016; Potter et al., 2012, 2013), we measure the radial distance between the thickened parts of the crust ("diameter of the largest crustal thickness" [$DLCT$]) and use this parameter as a measure of basin size both in our models and for the observed basins. In Supporting Information S1, we describe in more detail the method we used to determine the $DLCT$ in our hydro-code models.

The morphometric parameters in our model, such as the $DLCT$, have to be determined when the basin formation process is finished. However, in the numerical models, it is not clear, when the main dynamic motions have ceased as toward the end of a simulation small material movements take place and the target does not come to rest completely. Therefore, the $DLCT$ value depends to some extent on the model runtime. In Supporting Information S1, we demonstrate that the $DLCT$ value converges with the runtime in our models and provide estimates of the minimum runtime required to approximate $DLCT$ sufficiently.

2.4. Relationship Between Size of Bouguer Anomalies and Basin Size

Previous studies (e.g., Miljković et al., 2016; Wieczorek et al., 2013) used numerical formation and crustal thickness models showing that the prominent positive gravity anomaly results from a mantle uplift in the basin center (Figure 2, area A). With increasing radial distance, the basin center is surrounded by a thickened crustal part (Figure 2, area B) which affects the gravity low. Since the shape of the Bouguer gravity anomaly and the subsurface are related to each other, we measure the diameter of the gravity anomaly and the distance between the thickened crustal parts to determine the size of a basin. To do so, we relate the size of the Bouguer anomaly with the thickened part of our crust, represented by the $DLCT$. To measure the size of the modeled Bouguer anomaly, we measure twice the distance between the anomaly minimum and

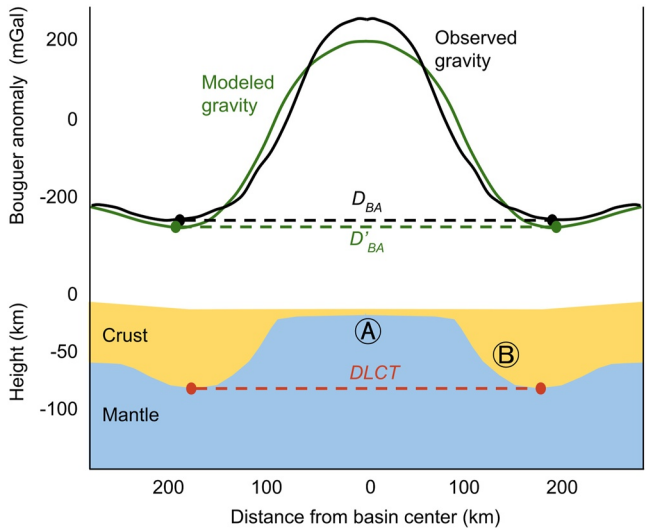

Figure 2. Schematic representation of how the parameters $DLCT$, D'_{BA}, and D_{BA} for basin size measurements: D'_{BA} and D_{BA} are measured between the minima of the modeled and the observed Bouguer anomalies and $DLCT$ is measured between the thickened crustal parts in the numerical model. (A) and (B) indicate the relevant subsurface structures that lead to the positive and negative amplitudes of gravity signatures.

the basin center. We define this as the "diameter of the modeled Bouguer anomaly" (D'_{BA}). Accordingly, we define the diameter of the Bouguer anomaly derived from the observed gravity signatures as D_{BA}.

2.5. Bouguer Gravity From Observations

In the next step, the Bouguer gravity was calculated for 16 basins on the lunar far side and related to the $DLCT$ from our models. Our basin selection is focused on impact structures with the characteristic positive anomaly in the center, surrounded by a gravity low. On the Moon's nearside, we can also find basins having the same "bulls-eye" patterns, but most of them are located within the mare regions. Since the mass distribution in mare regions emerges to be complex with dense basalts covering low-density anorthositic rock, we focus on basins located in the lunar highlands without any basaltic infill (Figure 3). Due to its special relevance and the good data basis, we also included the Orientale basin in our analysis. For estimating its Bouguer gravity signal (including the mare basaltic regions), we used the bulk density estimates provided by Zuber et al. (2016).

We applied a high-resolution gravity field model obtained by the GRAIL mission (Zuber et al., 2013), developed to spherical harmonic degree and order 1,500 (Park et al., 2015). The gravity field was truncated to an upper boundary of degree and order of 700 (corresponding to a spatial resolution of about 8 km), to account for high frequency noise and local differences in spatial resolution. We downward-continued the gravity field provided at a radius of 1,738 km to the mean radius of the topography (1,737.151 km). The topography was obtained by the Laser Altimeter Lunar Orbiter (LOLA) instrument (Smith et al., 2010) on-board of the Lunar Reconnaissance Orbiter (LRO). Together with lateral variations in bulk density of the upper crust (Wahl et al., 2020), the topography was used to calculate the Bouguer correction.

To compare the observed gravity with the results from our models, we created azimuthally averaged radial profiles of Bouguer gravity for each basin. Each point in the profile was estimated by calculating the mean

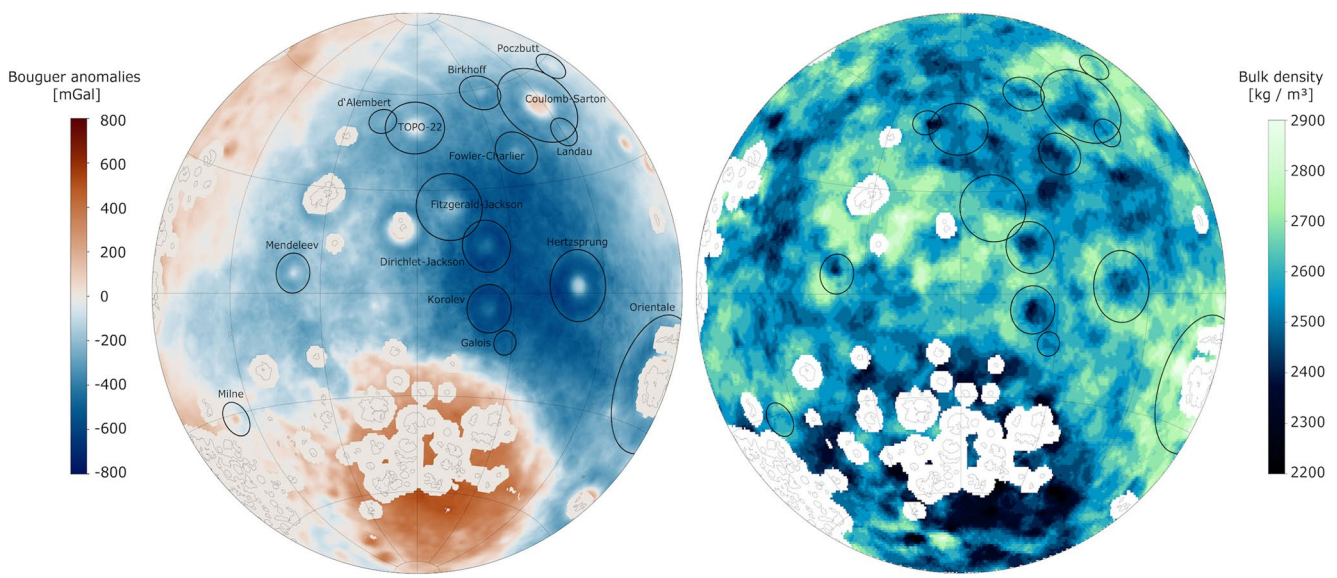

Figure 3. Bouguer gravity anomalies, referring to the mean radius of the topography (left) and bulk density of the upper crust (right) of the farside highlands. Both maps are given in Lambert conformal conic projection. The outer rims of investigated impact basins are marked with black circles; mare regions (Nelson et al., 2014) are surrounded in gray and were not part of the study (white areas).

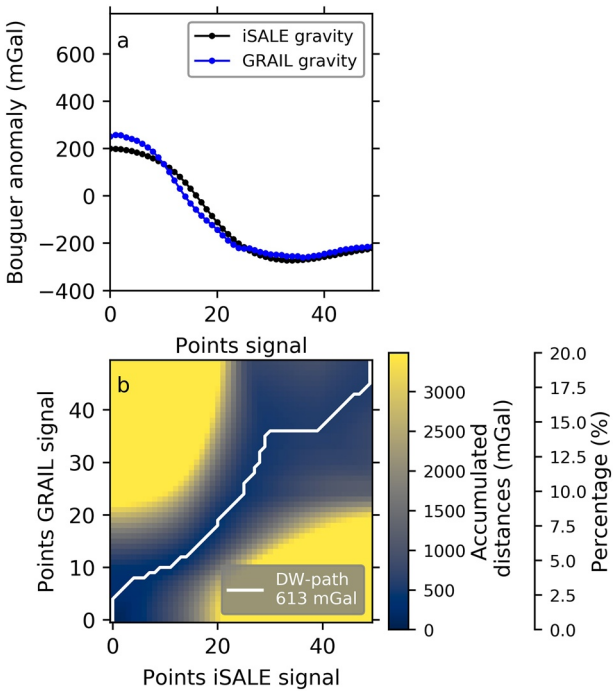

Figure 4. Schematic representation of using the DW-method for gravity forward modeling. (a) Measured gravity ("GRAIL gravity") and modeled gravity ("iSALE gravity") as a function of distance from basin center. Dots represent the gravity values between which the Euclidean distances are calculated in the DW-method. (b) Cumulative distance matrix with the optimal warping path (white line) as result of the DW-analysis. The matrix represents the accumulated distances that have been measured between all data points. The DW-path is derived by backtracking the smallest values in the cells, starting in the upper right and ending in the lower left corner of the matrix.

of all points with the same distance from the basin center. We also computed the standard deviation (shown in the gravity profiles in Figures S9–S24 in Supporting Information S1), which is the measure of the natural variability of any given point with respect to the mean value. For some candidates, the profile is affected by neighboring impact structures (e.g., Landau, D'Alembert). Here, only segments around the basins were considered, which are not influenced by interfering signals from adjacent basins (Table S2 in Supporting Information S1). The exact positions and dimensions of investigated basins were taken from Neumann et al. (2015).

2.6. Gravity Forward Modeling

To compare our basin formation models with the observed gravity anomaly, we model gravity signatures of individual basins based on the shape of the crust–mantle interface resulting from our numerical simulations. We assume a constant density in the crust and mantle to calculate gravity from the given mass distribution. The gravity anomaly calculation is performed using the approach as described in Supporting Information S1 of Collins (2014). To obtain a good fit with the observations, we vary the density of the crust (ρ_C) at different basins between 2,650 and 2,950 kg/m^3 in 100 kg/m^3 steps. The mantle density remains fixed in all models with a value of 3,314 kg/m^3. To eliminate the effect of the basin topography in the modeled gravity signature, we applied a Bouguer correction assuming the density equal to the used crustal density. The advantage of this approach is that the modeled gravity signal contains only information generated by the density contrast between crust and mantle, and, therefore, the gravity signal reflects the shape of the crust–mantle boundary. It should be noted that the applied Bouguer correction using crustal densities raises the amplitude of the modeled gravity signal in areas where mantle densities are predominant. This effect occurs mainly at the basin center, where the mantle comes close to the surface and the high densities predominate.

2.7. Model Fitting

In a final step, we directly compare the forward models based on the iSALE simulations with the observed gravity signature of basins. All investigated basins exhibit the Bouguer gravity anomaly with a pronounced positive peak at the basin center surrounded by a negative annulus (Figures 2 and 4a).

To find the best fit model from the suite of models with varying impactor diameter, crustal thickness, thermal profile, and crustal density, we correlate the modeled Bouguer gravity signal with the observed anomaly (Figure 4a). Classical quantitative correlation minimizes the area between the two curves with small areas indicating high correlation of the signals. However, this method does not necessarily consider the similarities of the signals in terms of their shape.

A well-established and more sophisticated method, for example, in seismology, to analyze the similarity of signals in a time–amplitude space, is the dynamic warping (DW) method (Müller, 2007, 2015), here applied to the distance–gravity space. In this method, described in more detail in Supporting Information S1, the Euclidean distances between the measured and the modeled signal are calculated pointwise. The obtained Euclidean distances are stored in a single distance matrix first. In a next step, we obtain a cumulative distance matrix (Figure 4b) from the single distance matrix which contains the sum of Euclidean differences of each pair of data points. This matrix is a measure for the similarity between the signals. Starting from the upper right corner in the accumulated matrix, the alignment path (Figure 4b) follows the smallest cumulative distances. The quality of the path is expressed by the accumulation of values for all cells it runs through. The warping path ("DW-path") is "good" if its total value is low and "bad" if its value is high. The

total value of an optimal warping path is named as "DW-distance." A small DW-distance is also a measure for a good similarity.

Diagonal running parts of the path indicate segments where the measured and modeled signals are running parallel and, thus, are highly similar regarding their trend. Vertical and horizontal running parts of the DW-path indicate changes between the trends of the signals relative to each other. In combination with the color distribution, which represents the cumulative distances (blue, small distances; yellow, large distances), we can judge whether we obtained a good or bad fit: we obtain a good fit when the DW-path runs diagonally through the entire matrix and is surrounded by a constant blue color pattern. The cells in the matrix turn yellow toward the upper left and lower right matrix corners. A continuous blue color implies that no distances are added to the last cumulative value. The diagonal running path represents high similarity between the signals. For all basins, we set the maximum of the color bars to the value that corresponds to 20% of the maximum cumulative distance value that is stored in the matrix (percentage scale next to the color bar in Figure 4b and Figures S9–S24 in Supporting Information S1) to obtain a better comparability between the DW-matrices. The analysis is computationally very efficient (to fit all basins, we need typically 45–60 min) and is applicable to large data sets of models (here: 3,456 gravity fits have been analyzed). The use of the DW-method itself is not limited by a smallest basin size. But in our case, we are interested in basins with prominent Bouguer anomalies characterized by a positive peak in the center and gravity lows at the sides. Therefore, the lower limit of basin size is defined by the smallest basin that still exhibits mantle uplift and, as a consequence, for which we found a gravity anomaly with a peak in the center and negative annulus around. Numerical models that do not provide crustal thickening anymore tend to be difficult to analyze because the negative anomaly is not so pronounced anymore. The smallest basins we investigated are Birkhoff, Galois, Milne, D'Alembert, and Poczobutt (Figures S9, S14, S16, S21, and S23 in Supporting Information S1).

3. Results

Our systematic numerical modeling study aims at finding relationships between the size of the observed basins and the mass of the impactor as a function of crustal thickness and thermal state of the Moon. Our results are constrained by the observed gravity anomaly and the proposed formation age of basins. Our results are constrained by the observed gravity anomaly and the proposed formation age of basins, which is comparable to the previous studies that only referred to impact basin sizes via the crustal thickness profiles (e.g., Miljković et al., 2016; Neumann et al., 2015).

3.1. Lunar Basin Sizes

In order to investigate whether the preimpact target temperature effects the excavation phase and the formation of the transient crater, we plot the scaled transient crater diameter π_D as a function of the gravity-scaled size π_2 for the three different thermal profiles and two crustal thicknesses (Figures 5a and 5b). The solid lines indicate π_2–π_D scaling relationship for Ottawa sand and competent (nonporous) rock according to, for example, Schmidt and Housen (1987), Holsapple and Schmidt (1987), and Melosh (1989). Note, the scaling line for nonporous rock has been proposed as the best experimental analog to predict transient crater size in solid rocks (Holsapple, 1993). First, we observe that our modeled transient crater diameters do not exactly follow the trend suggested by scaling but are closer to the line for nonporous rock than Ottawa sand. This is in agreement with previous studies (Miljković et al., 2016; Potter et al., 2015). The transient crater sizes in our models fall into two regimes: impactors larger than 40 km follow a steeper trend than smaller impactors. The two different scaling regimes are due to the layered target structure composed of crust and mantle with significantly different strength properties (see Figure 1b). With the increasing impactor size, the transient crater is increasingly more affected by the stronger mantle than the weaker crust. As we consider only impactors larger than 20 km in diameter, the transition between the two cratering regimes is only visible in Figure 5 for $L_{imp} < 40$ km in diameter. We speculate that for smaller impactors the π_D-trend in our models will roughly follow the scaling line for nonporous rock again but probably downshifted. The crustal thickness (Figures 5a and 5b) has some influence on π_D in our models but does not change the overall trend.

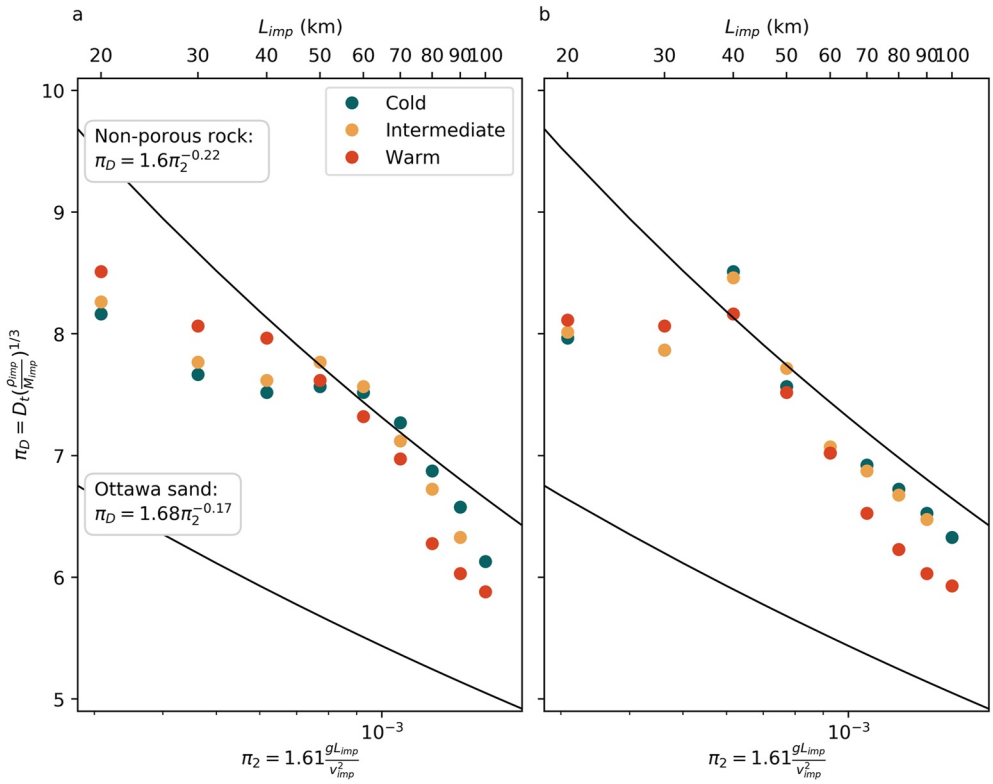

Figure 5. Scaled crater diameter (π_D) as a function of gravity-scaled size (π_2) for models with crustal thicknesses of 40 km (a) and 60 km (b) and different thermal conditions in the target (blue, cold; yellow, intermediate; orange, warm). The upper *x*-axis shows the corresponding impactor diameter (L_{imp}) if the gravitational acceleration is $g = 1.62$ m/s^2 and the impact velocity $v_{imp} = 13$ km/s.

Second, our models show that π_D also depends on the initial temperature of the target. Generally, the temperature effect on π_D is small for cold (blue circles) and intermediate (yellow circles) targets but much more pronounced for the warm case (orange circles). Although our results are a bit more scattered in case of the thinner crust (40 km) in comparison to the thicker crust (60 km), we find for both crustal thicknesses that for larger impactor diameters ($L_{imp} \geq 40$ km), where cratering is controlled by the properties of the mantle, the scaled crater diameter π_D is smaller for the warm case than for the cold/intermediate case. In contrast, π_D is slightly larger for the warm case in comparison to the cold/intermediate case for smaller impactors ($L_{imp} \leq 40$ km), where cratering is affected by the strength properties of both crust and mantle. We explain this by the fact that strength in the crust and upper mantle does not differ significantly for the six different cases (two crustal thicknesses and three temperature profiles) shown here.

Next, we investigate the influence of the preimpact thermal state of the target on the final crater size. As stated above, we use the diameter of the largest crustal thickness ($DLCT$) as a measure of final crater size. Figure 6 shows the transient crater diameter D_t, $DLCT$, D'_{BA}, and the ratios of $DLCT$ and D_t and $DLCT$ and D'_{BA} as functions of impactor size (see also Table S1 in Supporting Information S1). All values are shown for the three different thermal profiles and the two crustal thicknesses.

As for D_t (Figures 6a and 6f), $DLCT$ (Figures 6b and 6g) and D'_{BA} (Figures 6c and 6h) increase with increasing impactor size for both crustal thicknesses. The effect of the initial target temperature is more pronounced the larger the impactor diameter. Generally, impacts into a warm target result in larger $DLCT$ and D'_{BA} values compared to impacts into cold (blue) and intermediate (yellow) targets (Figures 6b, 6c, 6g, and 6h). Interestingly, this is the opposite trend that we observe for the transient crater diameter, where D_t tends to be smaller for warm targets than for intermediate/cold targets.

The temperature effect on crater formation becomes most obvious when plotting the $DLCT/D_t$-ratio as a function of impactor size (Figures 6d and 6i). As in the π_2–π_D-representation, the two cratering regimes

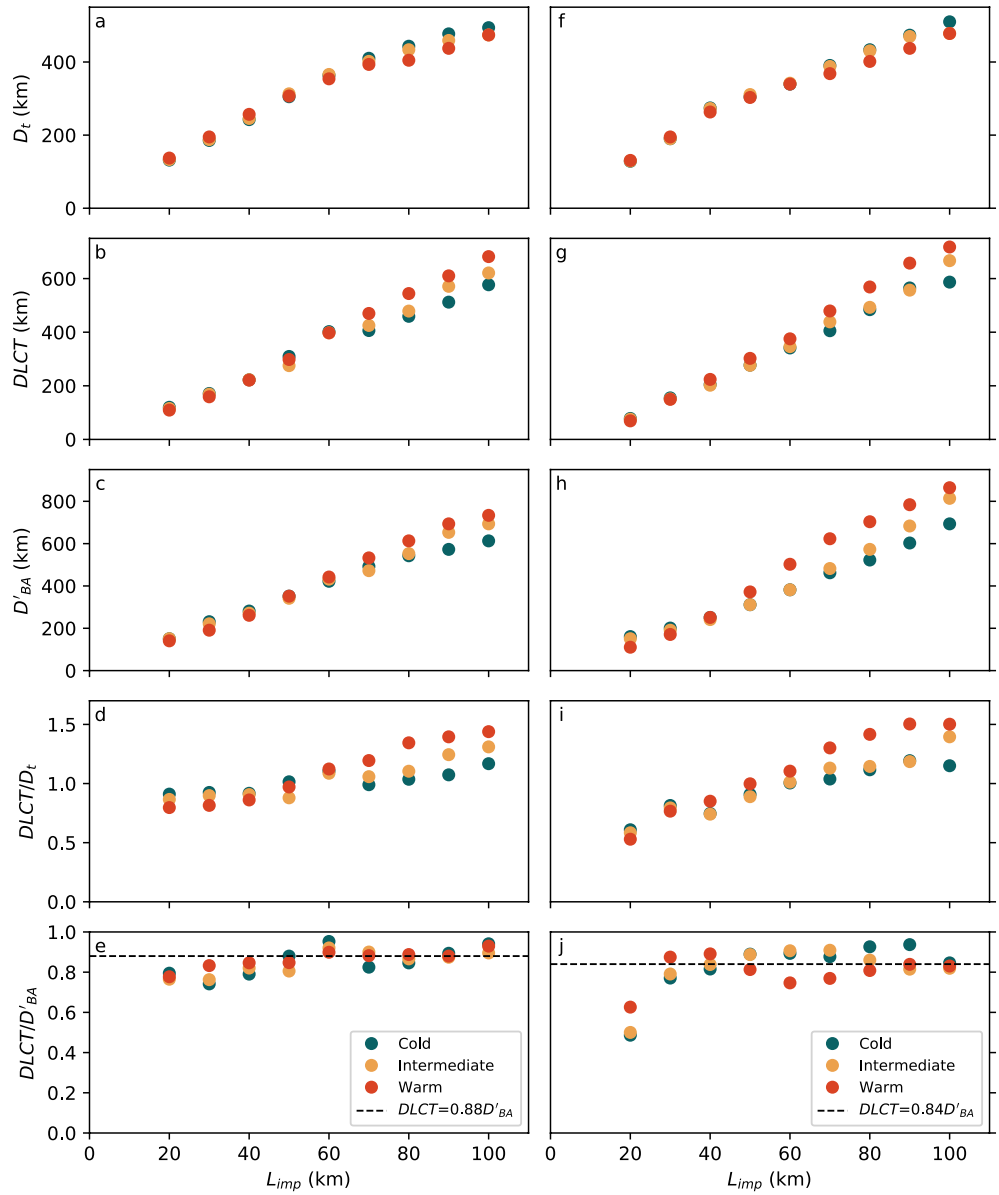

Figure 6. Results for two crustal thicknesses (a–e: 40 km, f–j: 60 km) and three thermal states (see legend). As a function of impactor size are shown: D_t (a, f), $DLCT$ (b, g), D'_{BA} (c, h), and the ratios of $DLCT$ and D_t (d, i) and $DLCT$ and D'_{BA} (e, j).

are visible: for $L_{imp} \geq 40$ km, $DLCT/D_t$ is larger in the warm case than in the cold/intermediate case. For $L_{imp} \leq 40$ km, the dependency of the ratio on temperature is less pronounced but the $DLCT/D_t$ tends to be smaller for warm than for intermediate/cold targets.

$DLCT$ as a function of D'_{BA} can be approximated by linear functions depending on the crustal thicknesses (equations in Figures 6e and 6j). From this relationship, we can derive the mean $DLCT/D'_{BA}$-values as 0.88 ($D_C = 40$ km) and 0.84 ($D_C = 60$ km), around which the ratios of $DLCT/D'_{BA}$ in Figures 6e and 6j are scattered (dashed lines). For this fitting, we neglect the thermal states since the data points are very close to one another.

The crustal thickness affects D_t, $DLCT$, and the ratios $DLCT/D_t$ and $DLCT/D'_{BA}$ much less, which is in agreement with Miljković et al. (2016). The two cratering regimes can be also distinguished by the morphology of the transient crater (see Figure S3 in Supporting Information S1): the shape of the transient

crater changes from flat (Figures S3a2–S3c2 and S3a3–S3c3 in Supporting Information S1) to bowl shaped (Figures S3f2–S3i2 and S3f3–S3i3 in Supporting Information S1), resulting in smaller transient craters with increasing impactor size for intermediate and warm thermal profiles. In comparison with Miljković et al. (2016), deviations regarding the size of the transient craters may result from the modified calculation of the transient crater diameter (after Manske et al., 2021) and the different thermal profiles for the lunar far side. However, apart from these small discrepancies, our results for the farside modeling regarding the $DLCT - D_t$ relationship are in agreement with Miljković et al. (2016).

3.2. Comparison of Modeled and Observed Gravity Signatures

Our systematic study of basin formation allows for a direct comparison with 16 existing basin structures on the lunar far side to find the models and corresponding set of parameters (impactor diameter, crustal thickness, and temperature profile) that best match the observations. We compare the observed gravity signal of each basin with the gravity signatures we determined for all models. Based on the analysis of the DW-matrix (e.g., Figure 7; blue colors indicate high similarity), we calculate the DW-path and the classical correlation (area between the curves). The model with the smallest value for both is considered as the best fit model. Both correlation parameters are listed for each basin in Table S3 in Supporting Information S1. Table 2 lists the best fit models, the corresponding set of parameters (impactor diameter, thermal profile, crustal thickness and density, and structure models are shown in Figures S9–S24 in Supporting Information S1), and derived diameter measurements.

As an example, we present our model for the Orientale basin (Figures 7d–7f). Orientale basin is one of the most studied basins (e.g., Johnson et al., 2016; Potter et al., 2013; Zhu et al., 2015) and shall serve as a benchmark to verify our approach here. Our analysis shows that an impactor with a size of 80 km and a cold lunar target with a 60 km thick crust and a velocity of 13 km/s reproduce the observed gravity anomaly of the Orientale basin the best (kinetic impact energy $E_{kin-ref} = 7.5 \cdot 10^{25}$ J). This result is in agreement with the study of Potter et al. (2013), who suggest an impactor diameter of 80 km at an impact velocity of 15 km/s ($E_{kin} = 1.3 \cdot E_{kin-ref}$). The study from Zhu et al. (2015) predicts an impactor size of 100 km and a velocity of 12 km/s ($E_{kin} = 1.6 \cdot E_{kin-ref}$). The best fit model matches the gravity signal for both assumed crustal thicknesses of 40 and 60 km arguing that Orientale is located at the border between the lunar highlands and the PKT. Both studies investigate the formation process of Orientale and have the same thermal profiles with a gradient of 10 K/km. The study of Johnson et al. (2016) focuses on Orientales ring structures and fault zones. They propose an impactor diameter of 64 km assuming a 53 km thick crust, a higher thermal gradient of 14 K/km, and an impact speed of 15 km/s ($E_{kin} = 0.7 \cdot E_{kin-ref}$).

For the Orientale and Hertzsprung basins, Figure 7 shows measured (solid black line) Bouguer anomalies (Figures 7a and 7d) compared with the corresponding iSALE models in dashed black line (Figures 7b and 7e). The matrices derived from the DW-analysis (Figures 7c and 7f) show the similarity between the signatures. The DW-path (white solid line; Figures 7c and 7f) follows the smallest distances and is a measure for the similarity between the compared signals. The almost diagonal shape of the DW-path together with blue colors indicates a high similarity between the signals. Small kinks occur due to small offsets between the signals. Outside the basin center, the minima of both Bouguer anomalies are positioned close to each other (Figures 7a and 7d). This shows that the measured gravity signal is related to the downward tilted crust between 240 and 330 km from the crater center for the Orientale basin (Figure 7b) and the stretched thickened part of the crust for the Hertzsprung basin (Figure 7e).

The matrix representation enables a comparison between the best fit models of all basins among another because the maximum of the color bars in Figures 7c and 7f is limited to the value corresponding to 20 % of the maximum cumulative distance value that is stored in the matrix. In both figures, the DW-path runs nearly diagonal. But differences between the best fit models are visible in the color distribution and the length of the DW-path: in Figure 7f, the blue is darker which represents the smaller distances, and the yellow areas around the DW-path show a nicer "waist" compared to the yellow areas in Figure 7c. Furthermore, the smaller DW-path value given in Figure 7f leads to the conclusion that the best fit model for the Orientale basin is better than the best fit model for the Hertzsprung basin. Based on the color pattern and

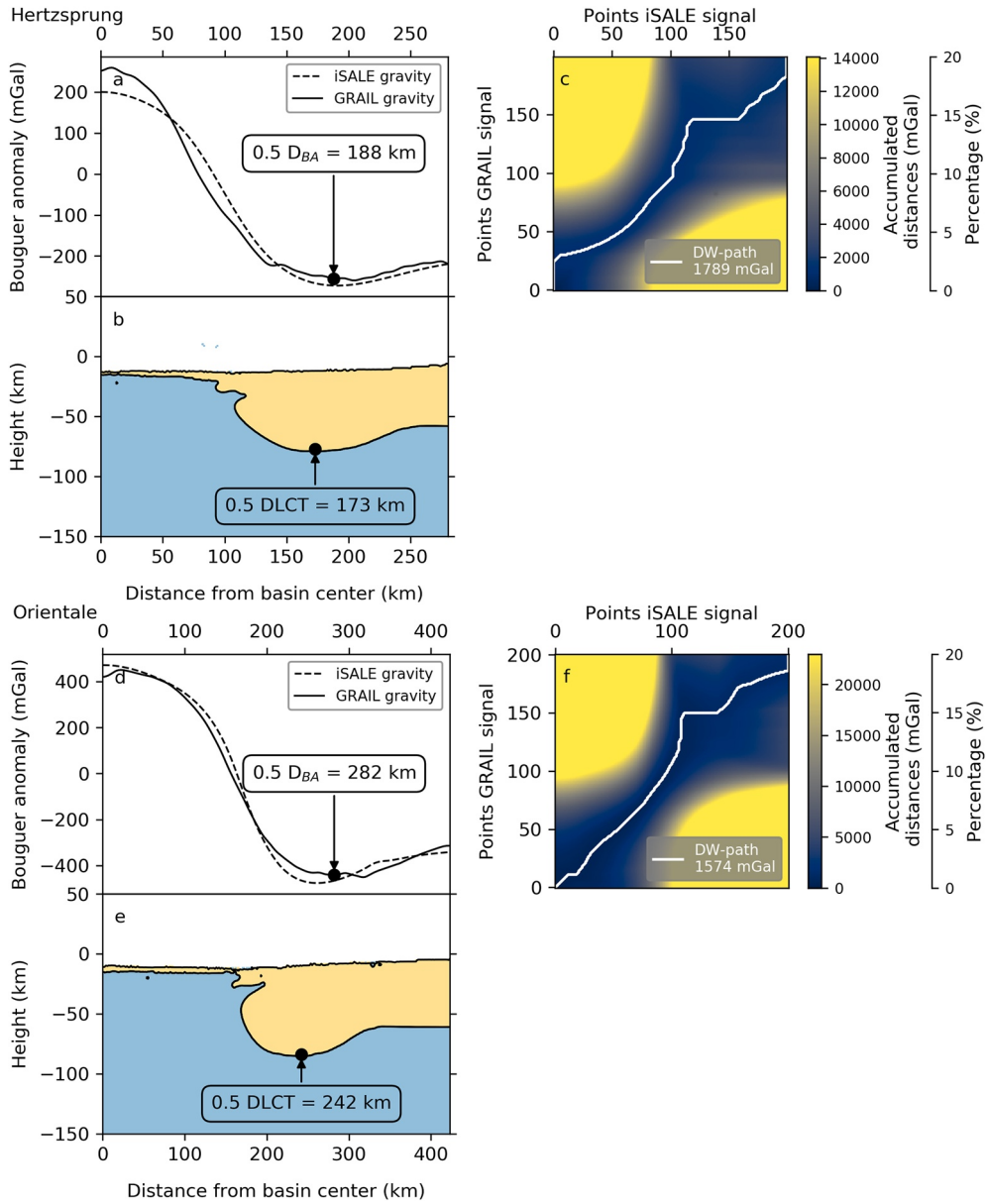

Figure 7. Comparison of the modeled (dashed black line) and measured (solid black line) Bouguer anomalies (a, d) with the corresponding iSALE model (b, e) for the Orientale and Hertzsprung basins. The color patterns of the accumulated distance matrix (c, f) derived from the DW-analysis show the similarity between the signatures. The DW-path (white solid lines) follows the smallest distances in (c) and (f) and its diagonal shape visualizes the similarity between the compared signals. The value of the DW-distance is also a measure for the offset between the signals.

the length of the DW-path, the quality of the parameters associated with the best fit models (D_t, $DLCT$ and D'_{BA}) can be evaluated.

3.3. Diameter Comparisons

The observed gravity signal reflects the present-day mass distribution, which is the result of mass displacement during the basin formation process and long-term isostatic equilibration and cooling effects. To relate observable parameters with modeling data, we show in Figure 8, the transient crater diameter D_t from our models as a function of the observed diameter of the Bouguer anomaly D_{BA}. At first glance, there appears

Table 2
Ages of Selected Lunar Farside Basins and Corresponding Numerical Model Parameters

	Basins	Center coordinates[a]		Formation time		Best fit model parameters				Modeled basin diameters			
No.	Name[b]	Latitude (°N)	Longitude (°E)	Age[c] (Ga)	Period[d]	T[e]	L_{imp} (km)	ρ_C (kg/m^3)	D_C (km)	D_{BA} (km)	$DLCT$ (km)	D_t (km)	D'_{BA} (km)
1	Birkhoff	58.9	213.4	$4.29^{+0.035}_{-0.047}$	PN	W	20	2,950	40	141	110	141	141
2	Fitzgerald-Jackson	25.1	190.6	$4.26^{+0.044}_{-0.063}$	PN(*)	I	60	2,950	40	423	398	366	432
3	Dirichlet-Jackson	13.4	201.8	$4.23^{+0.022}_{-0.026}$	PN(*)	I	40	2,950	40	301	223	245	272
4	Coulomb-Sarton	51.2	237.5	$4.23^{+0.025}_{-0.030}$	PN	I	40	2,750	40	262	223	246	271
5	Fowler-Charlier	39.5	218.0	N.D.[f]	PN	I	30	2,950	40	225	169	188	221
6	Galois	−14.0	207.7	N.D.[f]	PN	I	20	2,850	60	135	75	129	151
7	Landau	42.2	240.8	N.D.[f]	PN	I	30	2,950	60	171	151	190	191
8	Milne	−31.25	112.8	N.D.[f]	PN	I	20	2,850	40	166	115	133	151
9	Mendeleev	5.5	141.1	$4.13^{+0.044}_{-0.064}$	N; N/PN(*)	I	50	2,950	60	326	277	311	312
10	Korolev	−4.4	202.2	$4.11^{+0.021}_{-0.025}$	N; N/PN(*)	I	50	2,950	60	314	277	311	312
11	Hertzsprung	2.0	231.0	$4.09^{+0.030}_{-0.027}$	N; N/PN(*)	I	60	2,950	60	376	346	342	382
12	Orientale	−20.1	265.2	$3.81^{+0.0081}_{-0.008}$	LI	C	80	2,750	60	564	484	434	523
13	D'Alembert	51.05	164.8	N.D.[f]	N.D.[f]	I	20	2,750	60	130	75	129	151
14	Harkhebi	40.0	98.6	N.D.[f]	N.D.[f]	I	30	2,950	60	181	151	190	191
15	Poczobutt	57.7	260.4	N.D.[f]	N.D.[f]	W	20	2,950	40	123	109	137	141
16	TOPO-22	49.4	179.0	N.D.[f]	N.D.[f]	W	40	2,950	40	249	221	257	261

[a]Center coordinates for the basins adapted from Neumann et al. (2015), Table 1. [b]Basin nomenclatures are approved by the International Astronomical Union (IAU) or suggested by Neumann et al. (2015). [c]From Orgel et al. (2018), Table 2. [d]Periods from Wilhelms et al. (1987); if indicated with (*) periods taken from Fassett et al. (2011). [e]W, warm (ages ca. 4.4 Ga); I, intermediate (ages ca. 4.1 Ga); C, cold (ages ca. 3.8 Ga). [f]N.D., not determined.

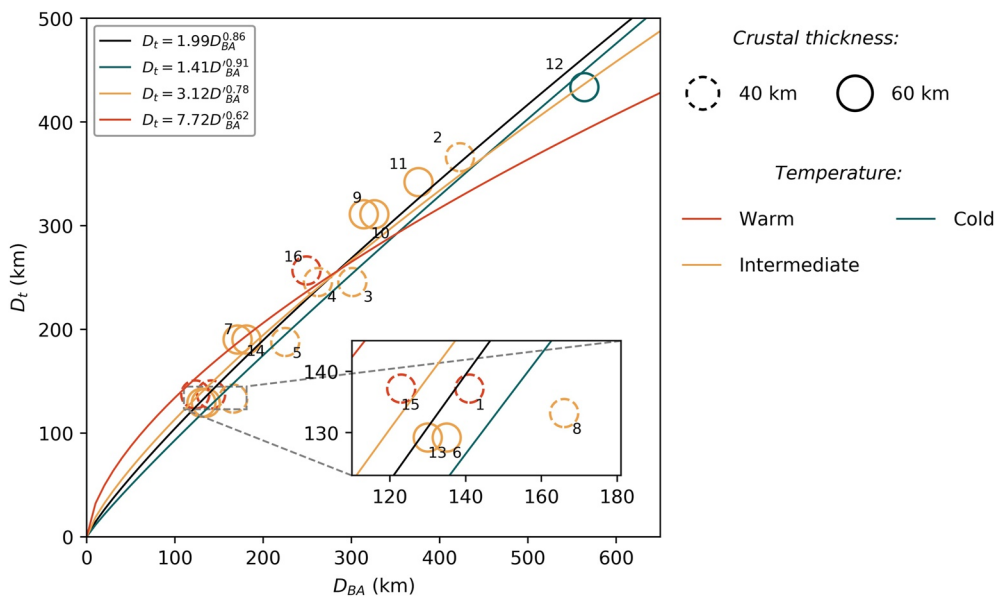

Figure 8. Modeled transient crater diameter as a function of observed Bouguer diameter. Colors of circles indicate the used thermal profiles in the models; styles of the circles depict different crustal thicknesses. Annotated numbers are related to the basins listed in Table 2.

to be an almost linear relationship between D_t and D_{BA}. Any effects due to different thermal profiles and different crustal thicknesses, as the π_2-π_D representation revealed (Figure 5), are barely noticeable.

As shown in Figure 6 for $L_{imp} \leq 40$ km the dependency of D_t on temperature is less pronounced than for larger impactors. Our best fit models predict impactors <50 km for 11 basins. Only five basins (No. 2, 9, 10, 11, and 12; Table 2) are formed by impactors of 50, 60 and 80 km in diameter, for which the temperature effect should be relevant. As noted above, the temperature effect of the warm and intermediate profile is very small (No. 2, 9, 10, and 11) and those four craters follow the linear trend (Figure 8). Only the Orientale basin (No. 12) was formed in a cold target and this is the only example that slightly deviates from the linear relationship between D_t and D_{BA}. Given the small number of basins formed by large impactors in cold targets, it is difficult to provide a clear trend that may depend slightly on target temperature. If we set the transient crater D_t in relation to the minimum of the modeled signal D'_{BA}, we can see a temperature effect that is particularly noticeable for impacts into warm material with large impactors (Figure 8, power laws for the three thermal states). The power laws are mainly dependent on the temperatures in the target, whereas the effect of crustal thickness is secondary.

Our data set consists of 16 D_{BA}-values, and, therefore, we are not able to derive individual thermal trends for the observed structures. For our observed basins, we fitted a power law,

$$D_t = 1.99 D_{BA}^{0.86} \tag{3}$$

to the available data neglecting the temperature effect. Combining this power law (Equation 3) with Figure 6 allows for estimating the impactor size from the observed Bouguer anomaly diameter D_{BA}. To give an example, the observed gravity anomaly with $D_{BA} = 400$ km leads to a D_t of 344 km (Figure 8 and Equation 3). Figure 6 then suggests for a transient crater diameter of 344 km an impactor size between 60 and 70 km, depending on the thermal field and crustal thicknesses. The corresponding $DLCT$ ranges between 400 and 500 km.

In the following step, we relate the observed gravity signature to the subsurface structure (crustal thickness model) from our models. Analogous to the calculations, we have performed for the $DLCT/D'_{BA}$ ratio (Figures 6e and 6j), we fitted a linear function,

$$DLCT = 0.85 D_{BA} \tag{4}$$

to the available data neglecting the temperature effect and the crustal thickness (Figure 9a). Figure 9b depicts the ratio of the observed $DLCT$ and D_{BA} from our models as a function of impactor size. Given the poor database that is dominated by basins that have been formed by $L_{imp} < 40$ km, it is difficult to derive reliable trends distinguishing between models with different crustal thicknesses and thermal profiles. For most basins, the $DLCT/D_{BA}$-ratio falls between 0.7 and 1.0 and, therefore, plots around the mean $DLCT/D_{BA}$-ratio of 0.85 according to the assumed linear relationship (Equation 4).

3.4. Chronological Classification of the Models

The thermal state at the time of impact is related to the cooling history of the Moon. In Figure 10, we show the $DLCT/D_{BA}$-ratio as a function of literature-ages based on crater counting. Here, we refer to model ages from the most recent work on basin dating by Orgel et al. (2018). Their data are aligned with absolute ages and the chronostratigraphic periods suggested by Wilhelms et al. (1987). Following Wilhelms et al. (1987), we categorize basins into periods: the time intervals from 4.55 to 3.92 Ga ("Pre-Nectarian" [PN] period), from 3.92 Ga (formation of Nectaris basin) to 3.85 Ga ("Nectarian" [N] period), from 3.85 Ga (formation of Imbrian basin) to 3.80 Ga ("Lower Imbrian" [LI] period), and from 3.80 Ga (end of formation of Orientale basin) to 3.20 Ga ("Upper Imbrian" [UI] period). In Table 2, we list the 16 basins with the associated periods after Wilhelms et al. (1987) and for some basins recommended formation periods after Fassett et al. (2012), together with new absolute model ages from Orgel et al. (2018).

Depending on the availability of dating information, we classify our basins into three types, which are basins that have (a) an absolute model age and an suggested formation period based on the crater chronology

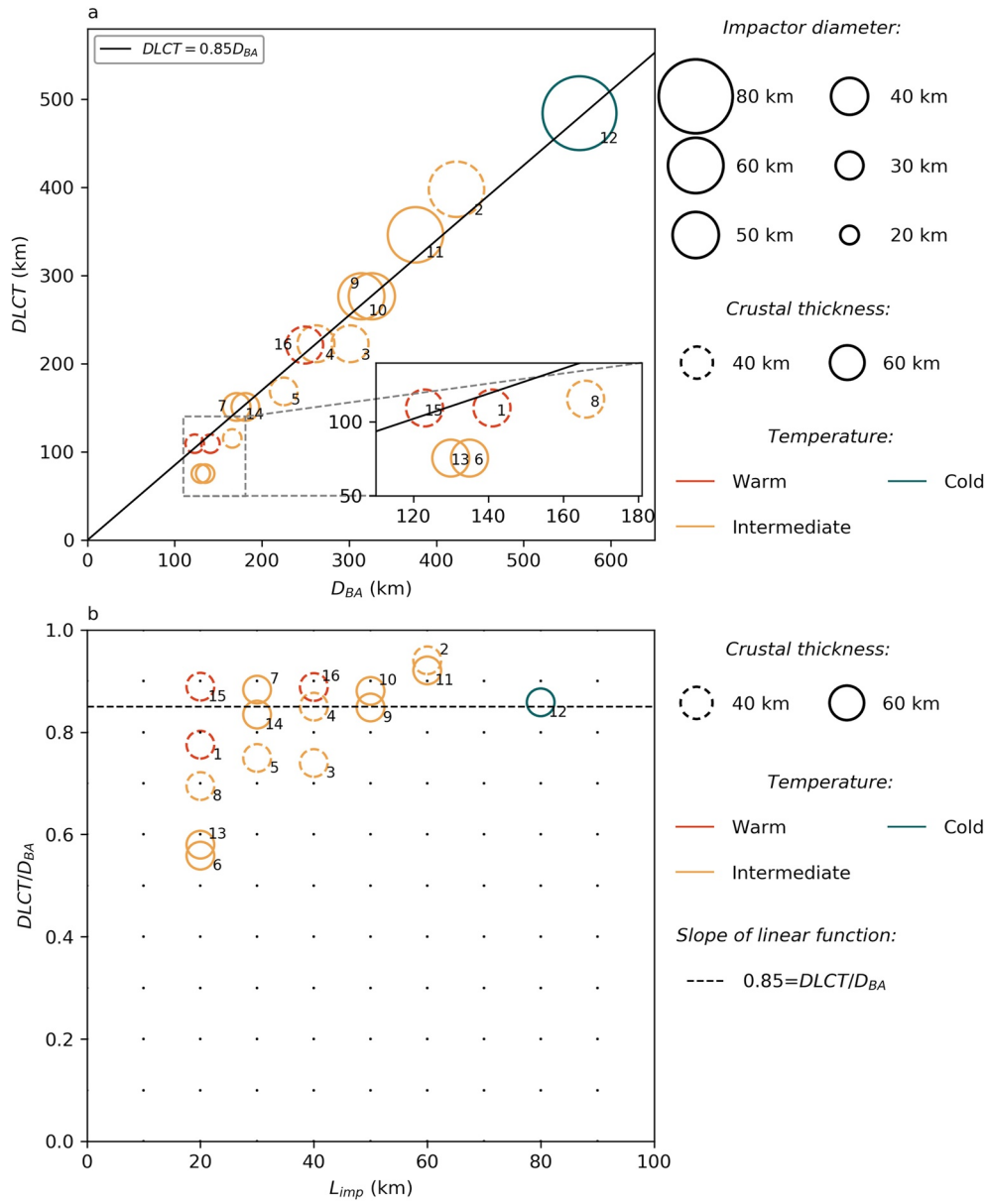

Figure 9. (a) *DLCT* as a function of D_{BA} with the corresponding linear fit. Colors of circles indicate the adopted thermal profiles in the models. Dashed or solid circles represent the two crustal thicknesses. Annotated numbers are related to the basins listed in Table 2. (b) Ratio of $DLCT/D_{BA}$ as a function of impactor size. Dashed black line indicates the mean ratio of $DLCT/D_{BA}$ (=slope of the linear function).

(e.g., Orientale), (b) no absolute model age but an entry in the crater chronology (e.g., Galois), or (c) neither an absolute model age nor an entry in the crater chronology (e.g., D'Alembert).

Vertical dashed lines in Figure 10 mark the time periods after Wilhelms et al. (1987). The hatched circles indicate the availability of absolute ages from crater counting (type a) for these basins. The data points are plotted at the estimated ages by Orgel et al. (2018). To give an example, Fitzgerald-Jackson (No. 2) is plotted at an age of 4.26 Ga according to Orgel et al. (2018). Basins that have no age are shown as open circles. For some basins (e.g., Milne [No. 8]), no absolute model ages are available but a classification regarding their formation period (type b). Suggested formation periods after Wilhelms et al. (1987) and Fassett et al. (2012) are indicated with horizontal lines crossing the data points. If no information about the formation period is available (basins No. 13, 14, 15, and 16), the period is shown from 4.55 to 3.20 Ga, to set a possible time range

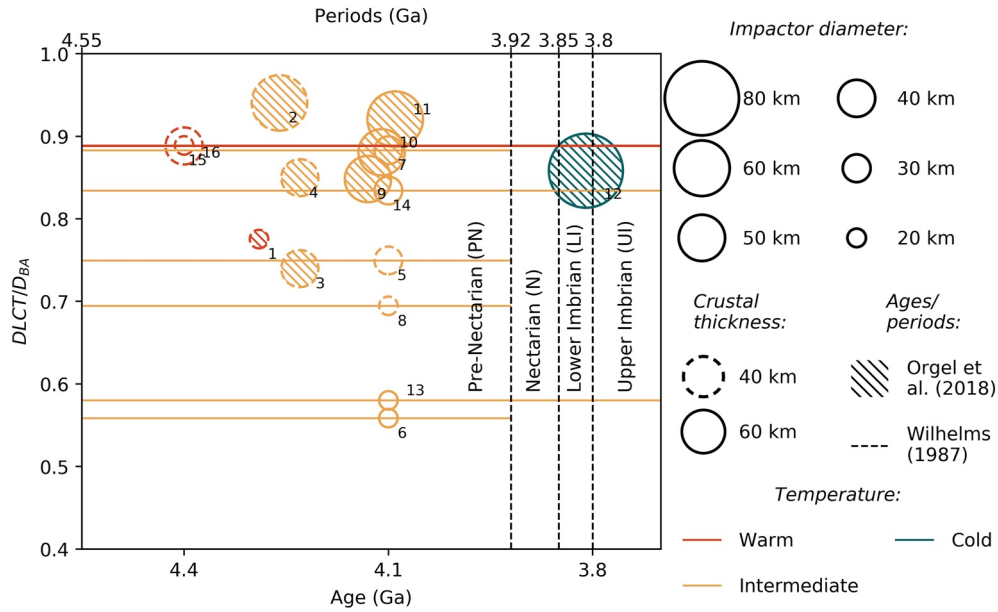

Figure 10. $DLCT/D_{BA}$-ratio as a function of time. The lower *x*-axis shows the ages related to the thermal evolution model; the crater chronology periods (Wilhelms et al., 1987) are indicated at the upper *x*-axis and by vertical dashed lines. Colors of circles and lines indicate the used thermal profiles in the models. The size of the circles represents used impactor diameters in the numerical models; line styles of the circles represent different crustal thicknesses. The hatched circles indicate that absolute ages from crater counting are available (Orgel et al., 2018). Horizontal lines through each data point indicate the period into which the basins are categorized after Wilhelms et al. (1987) and Fassett et al. (2012) when no ages from Orgel et al. (2018) are available.

of formation (type c). For the types b and c, the data points plot at the age related to the thermal profiles (3.8, 4.1, and 4.4 Ga). The colors of the circles indicate the used thermal profiles in the numerical models. Basins which are formed on a young and hot Moon plot close to 4.55 Ga, whereas basins formed later and in an already cooler lunar environment plot close to 3.80 Ga.

For 8 out of 16 basins, we have age determination from crater counting (Table 2 and hatched circles in Figure 10). The distribution in Figure 10 shows that models with intermediate and cold temperatures can be assigned to the respective ages of approximately 4.1 and 3.8 billion years. For this period, the largest number of basins is available, which are also dated with absolute ages. The temperature profiles used in the basin formation models correspond to the age information from Orgel et al. (2018): for the intermediate temperature profile, the ages spread from 4.09 Ga (Hertzsprung [No. 11]) to 4.26 Ga (Fitzgerald-Jackson [No. 2]). Birkhoff (No.1) has an assumed age of 4.29 Ga (Orgel et al., 2018) and is close to this range, but our best fit model suggests a warm thermal profile that was used in our simulation. The only basin that has been modeled with a cold thermal profile is Orientale (No. 12), which is also in line with the formation time after Orgel et al. (2018). The models for which no absolute age is available (type b) match the periods proposed by both Wilhelms et al. (1987) and Fassett et al. (2012) (e.g., Fowler-Charlier [No. 5]; Milne [No. 8]).

This figure clearly shows that an intermediate thermal setting was used for the modeling of the majority of the basins and that all basins can be classified in the period between 4.4 and 4.1 Ga. The temperature profiles we used in the models are related to the thermal evolution of the Moon and are in agreement with the results from crater counting analyzes.

Numerical models that predict impacts into a 40 km thick crust are performed for the basins Birkhoff, Fitzgerald-Jackson, Dirichlet-Jackson, Coulomb-Sarton, Fowler-Charlier, Milne, Poczobutt, and TOPO-22. To evaluate the results, we compare our preimpact thickness of 40 km with the crustal thickness profiles from Miljković et al. (2016, Supporting Information S1). Our assumed thickness is in agreement with their thicknesses for the range between 35 and 45 km for all basins, except Fitzgerald-Jackson and Dirichlet-Jackson with thicknesses of 50 km and Fowler-Charlier a thickness of ca. 48 km. Their crustal thicknesses are in between our assumed values of 40 and 60 km.

The basins Galois, Landau, Mendeleev, Korolev, Hertzsprung, Orientale, D'Alembert, and Harkhebi are modeled by assuming a 60 km thick crust. A comparison to Miljković et al. (2016) shows that the crustal thickness models predict thicker crusts compared to the presented basins before. Nevertheless, their predicted crusts range around 45–55 km in thickness, whereas our models assume 60 km. This comparison can only serve as a rough classification, since the crustal thickness models assume an average global crustal thickness of 34 km and, thus, comparisons with our local models with a 60 km thick crust are difficult. The crustal thickness models certainly suggest a larger variety in thickness between the investigated basins. Nevertheless, our results show that the effect of crustal thickness is small even if we assume the two extreme scenarios of a 40 and a 60 km thick crust.

4. Discussion

4.1. Bouguer Gravity of the Lunar Highlands From Observational Data

The high resolution of the applied GRAIL gravity model allows for a detailed analysis of the mass distribution of individual impact basins. To achieve the most accurate results calculating Bouguer gravity, we introduced locally variable bulk densities of the surface terrain of the upper few kilometers with an average of 4 km of the lunar crust.

In contrast to basin formation models providing absolute thicknesses of the crust, the Bouguer gravity anomalies may be interpreted to show the shape of the crust–mantle interface. Since the vertical mass distribution inside a planetary body derived from gravity data remains ambiguous, the crust–mantle interface cannot be assigned to a certain depth without defining further constraints, such as the average crustal thickness and the bulk density of the mantle rock.

Unlike previous work (e.g., Freed et al., 2014; Miljković et al., 2016; Zhu et al., 2015), our study focuses only on the gravity record of basins located in the lunar highlands, not showing any basaltic infill. Due to its special relevance being one of the youngest and best preserved basins on the Moon, we decided to include Orientale in our analysis, even though basaltic rock can be found in the center. Here, we use bulk density estimates provided by Zuber et al. (2016) for calculating the related Bouguer anomaly.

Mare basaltic regions on the Moon appear to be complex in their interior structure. Even if reliable assumptions for the bulk density of mare basalts may be derived from the laboratory examination of lunar rock samples, as well as from grain densities derived from global spectrometer data (together with the assumption of very low porosity for mare basalts), the main difficulty is the exact thickness of the mare basaltic infill. If an incorrect portion of the upper masses is subtracted from the gravity field signal when calculating the Bouguer correction, the resulting crust–mantle interface changes its shape (e.g., the expression of the mantle uplift in the center of lunar basins may be distorted). A detailed spatial distribution map of the basaltic rock is needed to estimate the amount of mare infill (Ding et al., 2021). By comparing the observed crater depth with the depth derived from scaling laws, assumptions on the mare thickness can be made. Ding et al. (2021) findings on mare basalt deposit distribution (e.g., only in the center or the whole crater region) may help to calculate more reliable Bouguer gravity anomalies of lunar nearside basins and to extend our forward modeling to impact structures filled with mare basalts.

4.2. Gravity Forward Modeling

To fit the observed and modeled gravity signatures, we use average constant densities in the crust between 2,650 and 2,950 kg/m^3, and a constant density in the mantle of 3,314 kg/m^3. The proposed crustal densities were chosen larger than today's average bulk density of the upper highland crust of 2,530 kg/m^3 (Wahl et al., 2020), assuming a lower porosity of the crustal rock at time of basin formation. Alternatively, it is also possible to use the density distribution in the crust and mantle from the iSALE simulation, which is rather complex. The density field represents the thermodynamic state immediately after impact: the subsurface of the structure is significantly heated as a consequence of shock compression and in particular an anvil-shape region underneath the central part is typically molten. The crustal densities in the heated and partially molten area tend to be lower than the assumed preimpact and observed postimpact densities because of thermal expansion. Especially inside the peak ring-radius, high crustal densities are observed (Wahl

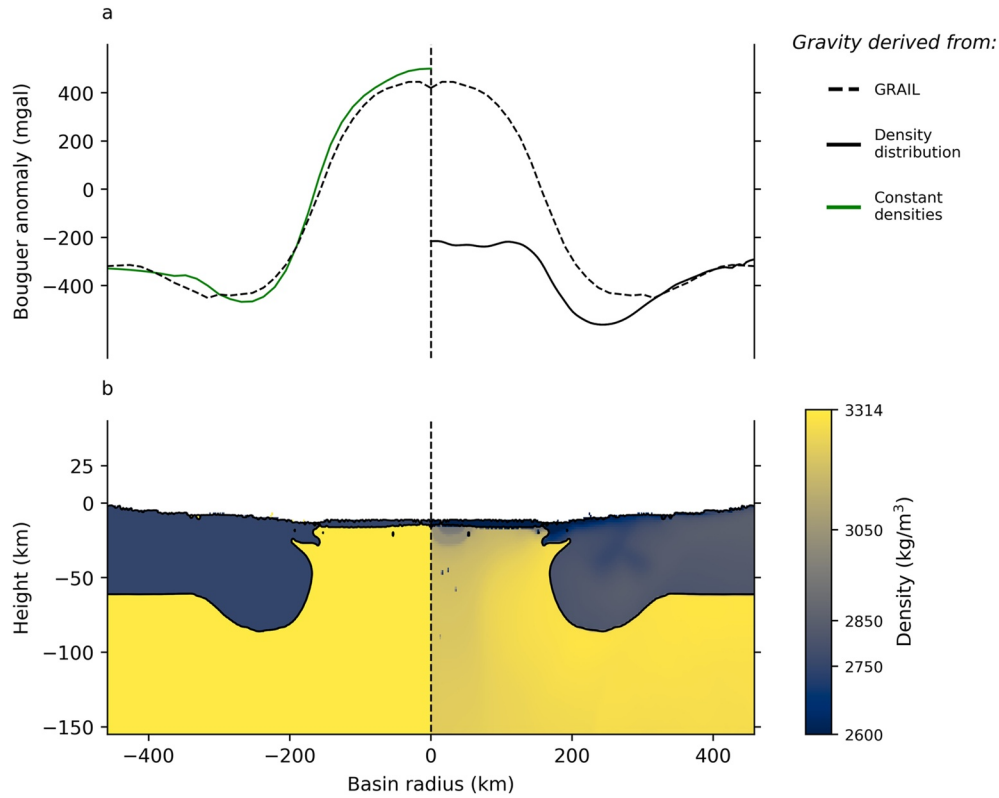

Figure 11. Section through the iSALE model (b) of the Orientale basin with constant densities in the target (ρ_{Mantle} = 3,314 kg/m^3, ρ_{Crust} = 2,750 kg/m^3) (left) and the modeled density distribution (right). In (a), the related gravity signals (green and black solid lines) in comparison to the observed gravity (dashed line) are shown.

et al., 2020), probably caused by cooling and recrystallization of impact melt, which is not taken into account in the models. We assume here that after cooling and recrystallization of impact melt the present-day density field may be better approximated by a mean crustal density as proposed above. Figure 11 shows the gravity anomalies of the Orientale basin derived from the density distribution at the end of an iSALE simulation (Figure 11b, right panel) and assuming a constant density (Figure 11b, left panel). Figure 11a shows the observed gravity (dashed line) in comparison with gravity responses from the iSALE model for the two different assumptions regarding the density distribution shown below (green and black solid lines). The lower amplitude of the gravity signature on the right side results from heated material with a lower density. The assumption to use a constant density accounts for the density increase as a consequence of cooling and recrystallization with time. Note, the $DLCT$, most important for the present study, remains the same, independent of the density distribution that has been assumed in the model.

Furthermore, the density of the crust may be modified through subsequent impacts. The mean best fit crustal densities ρ_C from our model (Table 2) are larger compared to the present-day densities of the highland crust, having a global mean of about 2,530 kg/m^3 (Wahl et al., 2020). However, impact cratering changes the initial porosity, and hence the initial bulk density of the crust (e.g., Milbury et al., 2015; Soderblom et al., 2015; Wahl et al., 2020). Smaller craters formed subsequently in the basin area presumably increased the porosity of the crustal material, which is why observed present-day densities are lower compared to the resulting densities from our numerical models.

Apart from cooling, basins may also have experienced isostatic adjustment (e.g., Freed et al., 2014; Melosh et al., 2013) which may lead to a modification in basin morphometry and change in gravity signature over time. The models, however, represent the pristine basin structures and their gravity right after formation. Our best fit models do not account for structural isostatic effects, for example, uplift processes, after the basin has formed. However, full equilibration may not have been reached at all basins. Freed et al. (2014) studied the effect of isostatic relaxation and showed that the basin center and the crustal annulus experiences

uplift due to a flexural uplift of the surrounding crust and the accompanying uplift of the basin floor during the cooling process. For two example basins, Freundlich-Sharonov and Mare Humorum, they show that the isostatic adjustment and cooling process only causes an increase in the amplitude in the center of the anomaly, whereas the position of the gravity minimum remains unchanged. In our analysis, the location of the Bouguer minimum is significant because its distance to the basin center defines the Bouguer diameter and our main findings regarding the proposed impactor size should not change significantly after isostatic adjustment.

The presented gravity forward modeling approach is limited by assuming vertical impacts producing axially symmetric basin structures. Recent simulations with iSALE-3D (Collins et al., 2020) suggest that oblique impacts may alter the mantle deformation beneath the basin center. As a consequence, an offset might occur between the center of the Bouguer anomaly, which is related to the mantle uplift, and the center of the crater, defined by the position of the crater rim. The deformation of the mantle uplift could lead to an asymmetry in the gravity signature but we expect that this effect is minor compared to the uncertainties in our azimuthally averaged gravity profiles. In the future, we plan to conduct 3D simulations to investigate the effect of impact angle on the asymmetry of the gravity signature relative to the center of a basin. However, previous modeling and observational studies on the position of the central peak relative to the geometric center have shown that deviations can occur either in downrange or uprange direction (Shuvalov, 2003) and generally seem to appear rather randomly (Ekholm & Melosh, 2001), likely because of preimpact geological heterogeneities. Nevertheless, it cannot be excluded that the impact angle causes some systematic excursion of the gravity signature out of the geometry center.

4.3. Lunar Basin Sizes

The results show that changes in basin formation and the final basin size depend mainly on target temperature and impactor size. Differences in the derived linear functions for the $DLCT/D'_{BA}$-ratio (equations in Figures 6e and 6j) are rather minor, and thus, our chosen crustal thicknesses have only a secondary effect on the basin formation process. In Figure 6, we see no significant outliers in the data for D'_{BA} and D_t, whereas the $DLCT$ values tend to scatter (e.g., $L_{imp} = 50$ and 60 km, $D_C = 40$ km). This scattering is more pronounced in the ratio plots where $DLCT$ is involved. These inaccuracies can be related to difficulties associated with the determination of $DLCT$. We obtain an average standard deviation of 5 km by considering all models (see Supporting Information S1 for determination of $DLCT$). For large basins, the crustal thickening is not very pronounced and the inwards dipping crust does not allow for a clear determination of the crustal bulging and, thus, the $DLCT$.

A parameter that can be determined easily in our models is the D'_{BA}-value. We derive a mean standard deviation for all models of 4 km. From our numerical modeling study, we can predict the $DLCT/D'_{BA}$-ratios of 0.84 and 0.88.

These constant ratios imply that the position of the gravity signal is directly coupled to the $DLCT$ and increases proportional to an increase of L_{imp}. The ratio shows that the $DLCT$ does not exactly match the position of D'_{BA} but is slightly shifted toward the basin center. The position of D'_{BA} is closely related to the transition zone from the inner basin area to the area where the crust regains its original thickness. This is in contrast to the predicted position of the thickest part of the crust in crustal thickness models, which is located below the Bouguer minimum. This finding demonstrates that it is important to consider the basin formation process with its changing thermal state and impactor properties to study the inner basin structure and size. Compared to crustal thickness models (e.g., Wieczorek et al., 2013), our models predict a more lateral extent of the crust toward the basin center and a complex basin structure characterized by: crustal thinning across the central part (mantle uplift) surrounded by an annular bulge; larger basins show an anvil shaped uplift structure with less pronounced crustal thickening. In these cases, the $DLCT$ corresponds to the inwards dipping crustal structure. Therefore, it has to be distinguished between whether parameters describing the subsurface structure (e.g., $DLCT$) have been determined from crustal thickness models derived from the observed gravity data or numerical simulation of basin formation constrained by the observed gravity data. We consider the latter to be more accurate as the formation process controlled by a temperature dependent rheology is taken into consideration as an additional constraint. The former only considers a rather simple assumption of the shape of the uplifted mantle for the interpretation of the observational

data record, whilst the latter takes into account constraints given by the crater formation process allowing for more complex mantle uplift morphologies.

4.4. Diameter Comparisons

The $DLCT$ as a function of the modeled gravity minimum position (D'_{BA}) is temperature dependent (Figures 6c and 6h) and we propose linear relationships (Figures 6e and 6j). From these relationships, we derived the mean $DLCT/D'_{BA}$ ratios as 0.88 and 0.84. Accordingly, we relate the $DLCT$ to the diameter of the observed Bouguer anomalies (D_{BA}; Figure 9) and determine an average ratio of 0.84, which is in agreement with the ratios from the models.

For most basins, the $DLCT/D_{BA}$ ratio plots around the mean $DLCT/D_{BA}$ ratio. However, for impactor diameters of 20 km, the ratio varies between 0.55 and 0.9. It has to be noted that the observed Bouguer profile for the basins with the smallest ratios of 0.55–0.6 (Galois, No. 6; D'Alembert, No. 13; see also Figures S14 and S21, respectively, in Supporting Information S1) deviates from the typical anomalies. The gravity signature may be distorted by subsequent impacts and/or more complex regional geological settings. In addition, the corresponding iSALE models do not show a distinct crustal annulus, which leads to an error-prone and imprecise determination of the $DLCT$ value and, therefore, limits the applicability of measuring $DLCT$, D_{BA}, and D'_{BA}.

A $DLCT/D_{BA}$-ratio of approximately 0.9 implies that the thickened crustal annulus in the numerical model corresponds to the minimum of the observed gravity anomaly. This suggests that the shape of the negative gravity amplitude reflects the mass distribution in this area. Our modeling studies provide evidence for this in Hertzsprung (No. 11), TOPO-22 (No. 16), Poczobutt (No. 15), Coulomb-Sarton (No. 4), and Orientale (No. 12) basins. Crustal thickness models are shown in Figures S19, S24, S23, S12, and S20 in Supporting Information S1.

By comparing our results with data from Miljković et al. (2016), we obtain differences in the estimated impactor diameter for a given basin. The average differences between the impactor sizes are 23%; for the basins 6, 7, and 9–12, we obtain differences of more than 30% in impactor size. The reasons for this are due to several respects: differences in thermal profiles, different impact velocities, and the usage of crustal thickness models to find models for observed structures. In order to guard against misunderstandings, it should be noted that the thermal profiles we use are relatively cold compared to the profiles in Miljković et al. (2016). The terms “warm,” “intermediate,” and “cold” refer here only to the lunar far side, the terms in Miljković et al. (2016) refer to the nearside, a global mean, and the far side hemisphere.

Compared to previous work, we also obtain different basin diameters, and, therefore, it is expected that the impactor diameters are different. This discrepancy emphasizes that it is difficult to determine the size of a basin clearly and/or to decide what is the right feature to be chosen as a proxy for the size.

4.5. Chronological Classification

We assume that the Bouguer minimum of the observed anomaly will not change its position significantly, and, therefore, the long-term modification processes do not entirely alter observational constraints making them less applicable. Based on this, our main finding is that during the cooling history of the Moon similar-sized impacts produced different gravity signatures and associated subsurface modifications of the crustal structure, and differences in basin size and other morphometric parameters. In other words, if the impactor size (for a constant density and velocity) would be known, our models allow for estimating the point in time in the cooling history of the Moon. Further implications of this study could be to translate geological ages of lunar basins to a projectile distribution with age.

However, since we assume only three different thermal profiles (corresponding to three different cooling ages) and the crustal thickness is not entirely negligible and certainly varies across the lunar highlands, this finding comes with large inaccuracies but is in principle in line with predicted formation ages from crater chronology age determinations. For basins for which we only have the formation period, we can model all basins in the estimated time frames (e.g., Fowler-Charlier [No. 5] with an intermediate profile [4.1 Ga] in the Pre-Nectarian system). It was also possible to model basins with ages from newer age dating methods.

As an example, we can ascribe the Orientale basin with a proposed age of 3.81 Ga in the Lower Imbrian phase and a cold thermal profile (3.8 Ga) in our simulations.

5. Conclusion

Our study shows that the size and morphometry of a basin depends foremost on impactor properties, such as the impactor size, mass, and the impact velocity; however, as shown here and in previous studies (e.g., Miljković et al., 2016; Potter et al., 2015), target properties, such as crustal thickness and thermal state, have a nonnegligible effect on the basin formation process.

Our numerical modeling study shows that even small differences in thermal evolution affect the basin formation process. Note, we do not account for the temperature contrast between the lunar nearside and far side that has been studied elsewhere (e.g., Miljković et al., 2016) but focus on the thermal evolution of the lunar lithosphere and its effect on basin formation on the far side.

Typical morphological characteristics of many basins have been partly or completely removed by subsequent impacts, aggravating the determination of morphological characteristics on the surface. We use the diameter of the largest crustal thickness ($DLCT$) as a measure of basin size because this region is better preserved than surface morphology and it can be easily measured in impact simulations. We show that $DLCT$ correlates with the diameter of the Bouguer gravity signature (D_{BA}) and, thus, can be considered as a parameter that is controlled by impactor size, thermal state of the target, and crustal thickness. Compared to the $DLCT$, the position of the gravity minimum can be defined unambiguously and is less error-prone.

Present-day Bouguer gravity anomalies characterize basin structures, both well preserved and severely altered, and thus are a powerful tool to measure the size of these structures. For 16 lunar farside basins, we introduced the DW method as an efficient way to compare the gravity signals from the numerical models with the observed data. The DW-path and the DW-matrix allow for a quantitative estimate of the similarity between the gravity signals and, thus, of the accuracy of the fit. In our study, the smallest basins are formed by impactors of 20 km in diameter which are the smallest impactors we considered in our numerical modeling. The size of the corresponding basins is between a minimum $DLCT$ of 75 km and the smallest D_{BA} of 123 km.

As a result from our gravity modeling, we estimate a range of impactor sizes and possible thermal states of the Moon upon impact that explains the formation of the present-day impact structure. In our simulations, we coupled thermal evolution models with the formation time of a basin and, therefore, were able to perform a chronological classification of our investigated basins. This classification is consistent with the ages and periods determined by crater chronology and dating.

The relationship between D_{BA} and the $DLCT$ supports the use of gravity anomalies as a measure of basin size. The change in gravity anomalies as a function of the initial temperature conditions in the target as well as a function of impactor sizes shows that the time of the impact plays an essential role for the size of the present-day anomaly.

The comparison with crater dating in our study clearly shows that taking temperature into account, impact structures can be classified according to their age. In further studies, it should be investigated to what extent previous impacts have changed the thermal field locally, which could affect the basin formation process of subsequent impacts. In addition, a better quantitative understanding of how isostatic relaxation processes and the cooling of impact heated matter has altered the pristine gravity signature of basins.

Data Availability Statement

The modeling in this work has been done using the iSALE "Dellen" shock-physics hydrocode. Stable releases of iSALE are available via https://isale-code.github.io/. Data and Supporting Information S1 used in this study are accessible in the repository Lompa et al. (2021). There, data can be accessed for each figure.

Acknowledgments
The authors gratefully thank the developers of iSALE-2D and the pySALEPlot tool. This work is funded by the Deutsche Forschungsgemeinschaft (DFG, German Research Foundation)-Project-ID 263649064-TRR 170. Miljković research is fully funded by the Australian Government through the ARC. The authors thank the associated editor Gareth Collins, an anonymous reviewer, and Meng-Hua Zhu for their helpful comments to improve the manuscript. Open access funding enabled and organized by Projekt DEAL.

References

Amsden, A. A., Ruppel, H. M., & Hirt, C. W. (1980). *SALE: A simplified ALE computer program for fluid flow at all speeds*. Los Alamos Scientific Lab. https://doi.org/10.2172/5176006

Andrews-Hanna, J. C., Head, J. W., Johnson, B. C., Keane, J. T., Kiefer, W. S., McGovern, P. J., et al. (2018). Ring faults and ring dikes around the Orientale basin on the Moon. *Icarus*, *310*, 1–20. https://doi.org/10.1016/j.icarus.2017.12.012

Baldwin, R. B. (1963). *The measure of the Moon*. University of Chicago Press.

Benz, W., Cameron, A. G. W., & Melosh, H. J. (1989). The origin of the Moon and the single-impact hypothesis III. *Icarus*, *81*(1), 113–131. https://doi.org/10.1016/0019-1035(89)90129-2

Chapman, C. R., & McKinnon, W. B. (1986). Cratering of planetary satellites. In J. A. Burns & M. S. Matthews (Eds.), *IAU Colloq. 77: Some background about satellites* (pp. 492–580). https://doi.org/10.2307/j.ctv1v3gr3r.15

Collins, G. S. (2014). Numerical simulations of impact crater formation with dilatancy. *Journal of Geophysical Research: Planets*, *119*, 2600–2619. https://doi.org/10.1002/2014JE004708

Collins, G. S., Melosh, H. J., & Ivanov, B. A. (2004). Modeling damage and deformation in impact simulations. *Meteoritics & Planetary Science*, *39*(2), 217–231. https://doi.org/10.1111/j.1945-5100.2004.tb00337.x

Collins, G. S., Melosh, H. J., Morgan, J. V., & Warner, M. R. (2002). Hydrocode simulations of Chicxulub crater collapse and peak-ring formation. *Icarus*, *157*(1), 24–33. https://doi.org/10.1006/icar.2002.6822

Collins, G. S., Patel, N., Davison, T. M., Rae, A. S. P., Morgan, J. V., Gulick, S. P. S., et al. (2020). A steeply-inclined trajectory for the Chicxulub impact. *Nature Communications*, *11*, 1480. https://doi.org/10.1038/s41467-020-15269-x

Ding, M., Soderblom, J. M., Bierson, C. J., & Zuber, M. T. (2021). Investigating the influences of crustal thickness and temperature on the uplift of mantle materials beneath large impact craters on the Moon. *Journal of Geophysical Research: Planets*, *126*, e2020JE006533. https://doi.org/10.1029/2020JE006533

Ekholm, A. G., & Melosh, H. J. (2001). Crater features diagnostic of oblique impacts: The size and position of the central peak. *Geophysical Research Letters*, *28*(4), 623–626. https://doi.org/10.1029/2000GL011989

Elbeshausen, D., Wünnemann, K., & Collins, G. S. (2009). Scaling of oblique impacts in frictional targets: Implications for crater size and formation mechanisms. *Icarus*, *204*(2), 716–731. https://doi.org/10.1016/j.icarus.2009.07.018

Fassett, C. I., Head, J. W., Kadish, S. J., Mazarico, E., Neumann, G. A., Smith, D. E., & Zuber, M. T. (2012). Lunar impact basins: Stratigraphy, sequence and ages from superposed impact crater populations measured from Lunar Orbiter Laser Altimeter (LOLA) data. *Journal of Geophysical Research*, *117*, E00H06. https://doi.org/10.1029/2011JE003951

Fassett, C. I., Head, J. W., Smith, D. E., Zuber, M. T., & Neumann, G. A. (2011). Thickness of proximal ejecta from the Orientale basin from Lunar Orbiter Laser Altimeter (LOLA) data: Implications for multi-ring basin formation. *Geophysical Research Letters*, *38*, L17201. https://doi.org/10.1029/2011GL048502

Freed, A. M., Johnson, B. C., Blair, D. M., Melosh, H. J., Neumann, G. A., Phillips, R. J., et al. (2014). The formation of lunar mascon basins from impact to contemporary form. *Journal of Geophysical Research: Planets*, *119*, 2378–2397. https://doi.org/10.1002/2014JE004657

Head, J. W. (1974). Orientale multi-ringed basin interior and implications for the petrogenesis of lunar highland samples. *The Moon*, *11*(3), 327–356. https://doi.org/10.1007/BF00589168

Head, J. W. (1977). Origin of outer rings in lunar multi-ringed basins: Evidence from morphology and ring spacing. In D. Roddy, R. Pepin, & R. Merrill (Eds.), *Impact and explosion cratering: Planetary and terrestrial implications* (pp. 563–573). Pergamon Press, Inc.

Holsapple, K. A. (1993). The scaling of impact processes in planetary sciences. *Annual Review of Earth and Planetary Sciences*, *21*(1), 333–373. https://doi.org/10.1146/annurev.ea.21.050193.002001

Holsapple, K. A., & Schmidt, R. M. (1987). Point source solutions and coupling parameters in cratering mechanics. *Journal of Geophysical Research*, *92*(B7), 6350–6376. https://doi.org/10.1029/JB092iB07p06350

Hüttig, C., Tosi, N., & Moore, W. B. (2013). An improved formulation of the incompressible Navier–Stokes equations with variable viscosity. *Physics of the Earth and Planetary Interiors*, *220*, 11–18. https://doi.org/10.1016/j.pepi.2013.04.002

Ivanov, B., Melosh, H., & Pierazzo, E. (2010). Basin-forming impacts: Reconnaissance modeling. In *Large meteorite impacts and planetary evolution IV* (pp. 29–49). https://doi.org/10.1130/2010.2465(03)

Johnson, B. C., Andrews-Hanna, J. C., Collins, G. S., Freed, A. M., Melosh, H. J., & Zuber, M. T. (2018). Controls on the formation of lunar multiring basins. *Journal of Geophysical Research: Planets*, *123*, 3035–3050. https://doi.org/10.1029/2018JE005765

Johnson, B. C., Blair, D. M., Collins, G. S., Melosh, H. J., Freed, A. M., Taylor, G. J., et al. (2016). Formation of the Orientale lunar multiring basin. *Science*, *354*(6311), 441–444. https://doi.org/10.1126/science.aag0518

Katz, R. F., Spiegelman, M., & Langmuir, C. H. (2003). A new parameterization of hydrous mantle melting. *Geochemistry, Geophysics, Geosystems*, *4*(9), 1073. https://doi.org/10.1029/2002GC000433

Laneuville, M., Taylor, J., & Wieczorek, M. A. (2018). Distribution of radioactive heat sources and thermal history of the Moon. *Journal of Geophysical Research: Planets*, *123*, 3144–3166. https://doi.org/10.1029/2018JE005742

Laneuville, M., Wieczorek, M. A., Breuer, D., & Tosi, N. (2013). Asymmetric thermal evolution of the Moon. *Journal of Geophysical Research: Planets*, *118*, 1435–1452. https://doi.org/10.1002/jgre.20103

Le Feuvre, M., & Wieczorek, M. A. (2011). Nonuniform cratering of the Moon and a revised crater chronology of the inner solar system. *Icarus*, *214*(1), 1–20. https://doi.org/10.1016/j.icarus.2011.03.010

Lompa, T., Wünnemann, K., Wahl, D., Padovan, S., & Miljković, K. (2021). *Replication data for: Numerical investigation of lunar basin formation constrained by gravity signature*. TRR170-DB. https://doi.org/10.35003/MCI3M3

Manske, L., Marchi, S., Plesa, A.-C., & Wünnemann, K. (2021). Impact melting upon basin formation on early Mars. *Icarus*, *357*, 114128. https://doi.org/10.1016/j.icarus.2020.114128

Marchi, S., Mottola, S., Cremonese, G., Massironi, M., & Martellato, E. (2009). A new chronology for the Moon and Mercury. *The Astronomical Journal*, *137*(6), 4936–4948. https://doi.org/10.1088/0004-6256/137/6/4936

Melosh, H. J. (1979). Acoustic fluidization: A new geologic process? *Journal of Geophysical Research*, *84*(B13), 7513–7520. https://doi.org/10.1029/JB084iB13p07513

Melosh, H. J. (1989). *Impact cratering: A geologic process* (Vol. *11*). Oxford University Press. (Provided by the SAO/NASA Astrophysics Data System).

Melosh, H. J., Freed, A. M., Johnson, B. C., Blair, D. M., Andrews-Hanna, J. C., Neumann, G. A., et al. (2013). The origin of lunar mascon basins. *Science*, *340*(6140), 1552–1555. https://doi.org/10.1126/science.1235768

Melosh, H. J., & Ivanov, B. A. (1999). Impact crater collapse. *Annual Review of Earth and Planetary Sciences*, *27*(1), 385–415. https://doi.org/10.1146/annurev.earth.27.1.385

Milbury, C., Johnson, B. C., Melosh, H. J., Collins, G. S., Blair, D. M., Soderblom, J. M., et al. (2015). Preimpact porosity controls the gravity signature of lunar craters. *Geophysical Research Letters*, *42*, 9711–9716. https://doi.org/10.1002/2015GL066198
Miljković, K., Collins, G. S., Wieczorek, M. A., Johnson, B. C., Soderblom, J. M., Neumann, G. A., & Zuber, M. T. (2016). Subsurface morphology and scaling of lunar impact basins. *Journal of Geophysical Research: Planets*, *121*, 1695–1712. https://doi.org/10.1002/2016JE005038
Miljković, K., Wieczorek, M. A., Collins, G. S., Laneuville, M., Neumann, G. A., Melosh, H. J., et al. (2013). Asymmetric distribution of lunar impact basins caused by variations in target properties. *Science*, *342*(6159), 724–726. https://doi.org/10.1126/science.1243224
Miljković, K., Wieczorek, M. A., Collins, G. S., Solomon, S. C., Smith, D. E., & Zuber, M. T. (2015). Excavation of the lunar mantle by basin-forming impact events on the Moon. *Earth and Planetary Science Letters*, *409*, 243–251. https://doi.org/10.1016/j.epsl.2014.10.041
Miljković, K., Wieczorek, M. A., Laneuville, M., Nemchin, A., Bland, P. A., & Zuber, M. T. (2021). Large impact cratering during lunar magma ocean solidification. *Nature Communications*, *12*, 5433. https://doi.org/10.1038/s41467-021-25818-7
Morbidelli, A., Marchi, S., Bottke, W. F., & Kring, D. A. (2012). A sawtooth-like timeline for the first billion years of lunar bombardment. *Earth and Planetary Science Letters*, *355–356*, 144–151. https://doi.org/10.1016/j.epsl.2012.07.037
Morbidelli, A., Nesvorny, D., Laurenz, V., Marchi, S., Rubie, D., Elkins-Tanton, L., et al. (2018). The timeline of the lunar bombardment: Revisited. *Icarus*, *305*, 262–276. https://doi.org/10.1016/j.icarus.2017.12.046
Müller, M. (2007). *Information retrieval for music and motion* [Monograph]. Springer-Verlag. https://doi.org/10.1007/978-3-540-74048-3
Müller, M. (2015). *Fundamentals of music processing: Audio, analysis, algorithms, applications* (1st ed.). Springer International Publishing. https://doi.org/10.1007/978-3-319-21945-5
Nelson, D. M., Koeber, S. D., Daud, K., Robinson, M. S., Watters, T. R., Banks, M. E., & Williams, N. R. (2014). Mapping lunar Maria extents and lobate scarps using LROC image products. In *Lunar and Planetary Science Conference* (Vol. *45*, p. 2861).
Neumann, G. A., Zuber, M. T., Wieczorek, M. A., Head, J. W., Baker, D. M. H., Solomon, S. C., et al. (2015). Lunar impact basins revealed by Gravity Recovery and Interior Laboratory measurements. *Science Advances*, *1*(9), e1500852. https://doi.org/10.1126/sciadv.1500852
Ohnaka, M. (1995). A shear failure strength law of rock in the brittle–plastic transition regime. *Geophysical Research Letters*, *22*(1), 25–28. https://doi.org/10.1029/94GL02791
Orgel, C., Michael, G., Fassett, C. I., van der Bogert, C. H., Riedel, C., Kneissl, T., & Hiesinger, H. (2018). Ancient bombardment of the inner solar system: Reinvestigation of the "fingerprints" of different impactor populations on the lunar surface. *Journal of Geophysical Research: Planets*, *123*, 748–762. https://doi.org/10.1002/2017JE005451
Padovan, S., Tosi, N., Plesa, A.-C., & Ruedas, T. (2017). Impact-induced changes in source depth and volume of magmatism on Mercury and their observational signatures. *Nature Communications*, *8*(1), 1945. https://doi.org/10.1038/s41467-017-01692-0
Park, R. S., Konopliv, A. S., Yuan, D. N., Asmar, S., Watkins, M. M., Williams, J., & Zuber, M. T. (2015). A high-resolution spherical harmonic degree 1500 lunar gravity field from the grail mission. In *AGU Fall Meeting Abstracts* (Vol. *2015*, p. G41B-01).
Pierazzo, E., Artemieva, N., Asphaug, E., Baldwin, E. C., Cazamias, J., Coker, R., et al. (2008). Validation of numerical codes for impact and explosion cratering: Impacts on strengthless and metal targets. *Meteoritics & Planetary Science*, *43*(12), 1917–1938. https://doi.org/10.1111/j.1945-5100.2008.tb00653.x
Pierazzo, E., Artemieva, N., & Ivanov, B. (2005). Starting conditions for hydrothermal systems underneath Martian craters: Hydrocode modeling. In *Large meteorite impacts III*. Geological Society of America. https://doi.org/10.1130/0-8137-2384-1.443
Poirier, J.-P. (1991). *Introduction to the physics of the Earth's interior* (1st ed.). Cambridge University Press.
Poirier, J.-P. (2000). *Introduction to the physics of the Earth's interior* (2nd ed.). Cambridge University Press. https://doi.org/10.1017/CBO9781139164467
Potter, R. W. K. (2012). *Numerical modelling of basin-scale impact crater formation* (Doctoral dissertation). https://doi.org/10.25560/9322
Potter, R. W. K., Kring, D. A., & Collins, G. S. (2015). Scaling of basin-sized impacts and the influence of target temperature. *Geological Society of America Special Papers*, *518*, SPE518-06. https://doi.org/10.1130/2015.2518(06)
Potter, R. W. K., Kring, D. A., Collins, G. S., Kiefer, W. S., & McGovern, P. J. (2012). Estimating transient crater size using the crustal annular bulge: Insights from numerical modeling of lunar basin-scale impacts. *Geophysical Research Letters*, *39*, L18203. https://doi.org/10.1029/2012GL052981
Potter, R. W. K., Kring, D. A., Collins, G. S., Kiefer, W. S., & McGovern, P. J. (2013). Numerical modeling of the formation and structure of the Orientale impact basin. *Journal of Geophysical Research: Planets*, *118*, 963–979. https://doi.org/10.1002/jgre.20080
Schmidt, R. M., & Housen, K. R. (1987). Some recent advances in the scaling of impact and explosion cratering. *International Journal of Impact Engineering*, *5*(1), 543–560. https://doi.org/10.1016/0734-743x(87)90069-8
Shuvalov, V. (2003). Displacement of target material during impact cratering. In C. Koeberl & F. C. Martínez-Ruiz (Eds.), *Impact markers in the stratigraphic record* (pp. 121–135). Springer. https://doi.org/10.1007/978-3-642-55463-6_5
Smith, D. E., Zuber, M. T., Jackson, G. B., Cavanaugh, J. F., Neumann, G. A., Riris, H., et al. (2010). The Lunar Orbiter Laser Altimeter investigation on the Lunar Reconnaissance Orbiter mission. *Space Science Reviews*, *150*(1), 209–241. https://doi.org/10.1007/s11214-009-9512-y
Smith, D. E., Zuber, M. T., Neumann, G. A., Mazarico, E., Lemoine, F. G., Head, J. W., III, et al. (2017). Summary of the results from the Lunar Orbiter Laser Altimeter after seven years in lunar orbit. *Icarus*, *283*, 70–91. https://doi.org/10.1016/j.icarus.2016.06.006
Soderblom, J. M., Evans, A. J., Johnson, B. C., Melosh, H. J., Miljković, K., Phillips, R. J., et al. (2015). The fractured Moon: Production and saturation of porosity in the lunar highlands from impact cratering. *Geophysical Research Letters*, *42*, 6939–6944. https://doi.org/10.1002/2015GL065022
Spohn, T., Konrad, W., Breuer, D., & Ziethe, R. (2001). The longevity of lunar volcanism: Implications of thermal evolution calculations with 2D and 3D mantle convection models. *Icarus*, *149*(1), 54–65. https://doi.org/10.1006/icar.2000.6514
Thompson, S. L., & Lauson, H. S. (1974). Improvements in the CHART D radiation-hydrodynamic code III: Revised analytic equations of state. In *Report SC-RR-71 0714* (p. 119). Sandia Laboratories.
Wahl, D., Wieczorek, M. A., Wünnemann, K., & Oberst, J. (2020). Crustal porosity of lunar impact basins. *Journal of Geophysical Research: Planets*, *125*, e2019JE006335. https://doi.org/10.1029/2019JE006335
Wieczorek, M. A., Neumann, G. A., Nimmo, F., Kiefer, W. S., Taylor, G. J., Melosh, H. J., et al. (2013). The crust of the Moon as seen by grail. *Science*, *339*(6120), 671–675. https://doi.org/10.1126/science.1231530
Wilhelms, D. E., McCauley, J. F., & Trask, N. J. (1987). The geologic history of the Moon. *USGS Professional Paper*. https://doi.org/10.3133/pp1348
Wünnemann, K., Collins, G., & Melosh, H. (2006). A strain-based porosity model for use in hydrocode simulations of impacts and implications for transient crater growth in porous targets. *Icarus*, *180*(2), 514–527. https://doi.org/10.1016/j.icarus.2005.10.013
Wünnemann, K., Collins, G., & Osinski, G. (2008). Numerical modelling of impact melt production in porous rocks. *Earth and Planetary Science Letters*, *269*(3), 530–539. https://doi.org/10.1016/j.epsl.2008.03.007

Wünnemann, K., & Ivanov, B. (2003). Numerical modelling of the impact crater depth–diameter dependence in an acoustically fluidized target. *Planetary and Space Science*, *51*(13), 831–845. https://doi.org/10.1016/j.pss.2003.08.001

Zhu, M.-H., Wünnemann, K., & Potter, R. W. K. (2015). Numerical modeling of the ejecta distribution and formation of the Orientale basin on the Moon. *Journal of Geophysical Research: Planets*, *120*, 2118–2134. https://doi.org/10.1002/2015JE004827

Zuber, M. T., Smith, D. E., Neumann, G. A., Goossens, S., Andrews-Hanna, J. C., Head, J. W., et al. (2016). Gravity field of the Orientale basin from the Gravity Recovery and Interior Laboratory mission. *Science*, *354*(6311), 438–441. https://doi.org/10.1126/science.aag0519

Zuber, M. T., Smith, D. E., Watkins, M. M., Asmar, S. W., Konopliv, A. S., Lemoine, F. G., et al. (2013). Gravity field of the Moon from the Gravity Recovery and Interior Laboratory (GRAIL) mission. *Science*, *339*(6120), 668–671. https://doi.org/10.1126/science.1231507